

Title

Locus coeruleus neuromelanin predicts ease of attaining and maintaining neural states of arousal

Authors and Affiliations

Sana Hussain¹, Isaac Menchaca¹, Mahsa Alizadeh Shalchy³, Kimia Yaghoubi³, Jason Langley², Aaron R. Seitz³, Xiaoping P. Hu^{1,2†}, Megan A. K. Peters^{1,4†}

1. Department of Bioengineering, University of California Riverside, Riverside, CA
2. Center for Advanced Neuroimaging, University of California, Riverside, Riverside, CA
3. Department of Psychology, University of California Riverside, Riverside, CA
4. Department of Cognitive Sciences, University of California Irvine, Irvine, CA

†These authors contributed equally to this work

Sana Hussain ORCID: 0000-0003-0986-2654; email: shuss006@ucr.edu
Isaac Menchaca ORCID: 0000-0003-2912-2178; email: imenc001@ucr.edu
Mahsa Alizadeh Shalchy ORCID: 0000-0002-6576-9115; email: maliz001@ucr.edu
Kimia Yaghoubi ORCID: 0000-0002-6806-2617; email: kyagh001@ucr.edu
Jason Langley ORCID: 0000-0001-9412-1265; email: jason.langley@ucr.edu
Aaron R. Seitz ORCID: 0000-0003-4936-9303; email: aseitz@ucr.edu
Xiaoping P. Hu ORCID: 0000-0001-7014-5983; email: xhu@engr.ucr.edu
Megan A. K. Peters ORCID: 0000-0002-0248-0816; email: megan.peters@uci.edu

Word count: 10,609 (excluding abstract, references, figure captions, and appendices)
Figures/Tables: 7 Figures/7 Tables (excluding appendices)

‡Correspondence should be addressed to:

Megan A. K. Peters, Ph.D.
Assistant Professor, Cognitive Sciences, University of California, Irvine
Social & Behavioral Sciences Gateway 2314
Phone: (949) 824-6692
Fax: (949) 824-2307
E-mail: megan.peters@uci.edu

Xiaoping P. Hu, Ph.D.
Provost Fellow
Professor and Chair, Department of Bioengineering, University of California, Riverside
Materials Science and Engineering 205
Phone: (951) 827-2925
Fax: (951) 827-6416
E-mail: xhu@engr.ucr.edu

Abstract

The locus coeruleus (LC), a small subcortical structure in the brainstem, is the brain's principal source of norepinephrine. It plays a primary role in regulating stress, the sleep-wake cycle, and attention, and its degradation is associated with aging and neurodegenerative diseases associated with cognitive deficits (e.g., Parkinson's, Alzheimer's). Yet precisely how norepinephrine drives brain networks to support healthy cognitive function remains poorly understood – partly because LC's small size makes it difficult to study noninvasively in humans. Here, we characterized LC's influence on brain dynamics using a hidden Markov model fitted to functional neuroimaging data from healthy young adults across four attention-related brain networks and LC. We modulated LC activity using a behavioral paradigm, and also measured individual differences in LC neuromelanin. The model revealed five hidden states, including a stable 'arousal' state that occurred when subjects actively engaged with the task. LC neuromelanin correlated with this state's stability across experimental manipulations, and with subjects' propensity to enter into and remain in this state. These results provide new insight into LC's role in driving spatiotemporal neural patterns associated with attention and arousal, and demonstrate that neuromelanin variation can explain individual differences in these patterns even in healthy young adults.

Keywords

Locus coeruleus; hidden Markov model; brain states; norepinephrine; attention; fMRI

1. Introduction

The locus coeruleus (LC) circuit is the main source of norepinephrine (NE) in the brain; it projects to the entire brain and is deeply involved in cognitive functions related to arousal including attention, stress, and the sleep-wake cycle (Aston-Jones and Cohen, 2005; Chen et al., 2014; Guedj et al., 2017; Langley et al., 2017; Sara, 2009; Song et al., 2017). For example, LC degradation, prevalent in normal aging, is thought to impair memory and cause cognitive reserve depreciation (Mather and Harley, 2016), and LC dysfunction is hypothesized to occur in prodromal stages of Alzheimer's and Parkinson's diseases (Braak et al., 2011, 2003). In normal cognition, relationships among LC activity, arousal, attention, and performance have long been observed and are now classically characterized by the Yerkes-Dodson curve (Aston-Jones and Cohen, 2005): Moderate LC firing rates correspond to optimal task performance while low and high LC firing rates are associated with inadequate task performance because subjects are inattentive and distracted, respectively (Aston-Jones and Cohen, 2005).

But *how* do fluctuations in norepinephrine (due to fluctuations in LC activity) drive changes in brain states? Despite many observed correlations between LC activity and attention, the underlying mechanisms driving changes in network dynamics within this relationship are still not well understood (Aston-Jones and Cohen, 2005; Sara, 2009; Song et al., 2017). Characterizing these underlying mechanisms by studying normal cognition and LC behavior using computational models could provide foundational insight not only into healthy cognition, but also into disease states where LC structure and function is known to break down (Braak et al., 2011, 2003).

One primary measure of interest in developing such computational frameworks would be fluctuations in the LC itself, of course. This is highly challenging in awake, behaving humans in a noninvasive manner because of the extremely small size of the LC. The LC is only about 2 mm in diameter (**Figure 1**), meaning that even with recent advances in functional magnetic resonance imaging (fMRI) technology, LC blood oxygen level dependent (BOLD) signal can be incredibly noisy, as LC BOLD has been shown to be especially susceptible to noise due to cardiac pulsation and respiration (Clewett et al., 2016; Glover et al., 2000; Liu et al., 2017; Mather et al., 2017). Difficulties in accurately and precisely measuring the BOLD signal in LC render even sophisticated methods ineffectual. Seeking to quantify functional connectivity with LC, or using LC as a seed region for psychophysiological interactions analysis (O'Reilly et al., 2012), for example, might simply discover covariations with noise.

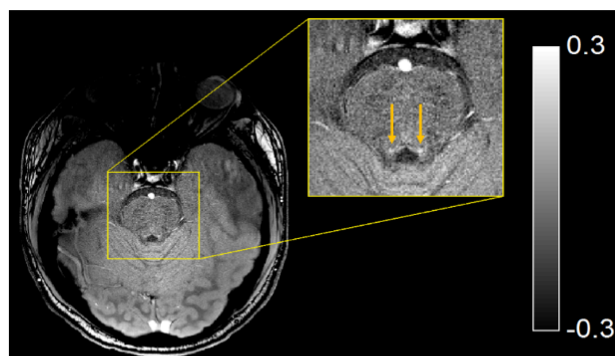


Figure 1. Neuroanatomical location of the locus coeruleus as seen in a neuromelanin-sensitive image. The locus coeruleus (LC) is a 2mm diameter nucleus located in the brainstem, here illustrated by the two dots on either side of the region

anterior to the fourth ventricle (Chen et al., 2014; Langley et al., 2017). The arrows indicate the position of LC.

To complicate matters more, there also exist individual differences in the neuronal density of LC even in young people (Keren et al., 2009). Although we are unaware of any documented relationships between memory performance and LC microstructure in younger adults (Langley et al., 2021, 2020; Mather and Harley, 2016) and neuronal loss in young adults is expected to be minimal if present at all (Manaye et al., 1995; Shibata et al., 2006; Zucca et al., 2006), variations in LC neuronal density may nevertheless lead to individual differences in the effectiveness (or effect size) of any manipulation designed to elicit fluctuations in LC activity, reducing group-level effect sizes further due to heteroscedasticity in post-manipulation behaviors across subjects.

One possible solution to these challenges is to use computational models that uncover and characterize repeating patterns in activity-based brain states, i.e. spatial patterns of co-activation that cycle repeatedly over a period of time. A popular tool for discovering these brain states is the hidden Markov model (HMM). HMMs can be used to discover patterns in complex, dynamic datasets, and are commonly used for weather prediction, in computational biology, and in finance (Eddy, 2004; Khatani and Ghose, 2017; Zhang et al., 2019); recently, HMMs are becoming more popular in neuroimaging. Neuroimaging-based HMMs identify latent brain states which quantify network or nodal interaction as well as the probability of transitioning between those hidden states (Baker et al., 2014; Chen et al., 2016; Eavani et al., 2013; Lindquist et al., 2007; Liu et al., 2014; Ou et al., 2015; Robinson et al., 2010; Shappell et al., 2019; Stevner et al., 2019; Vidaurre et al., 2018a, 2018b, 2017, 2016). As a result, an HMM could be applied to fMRI data to identify the spatiotemporal behavior of latent brain states as a function of arousal or LC up-regulation overall, rather than simply covariation with LC BOLD signal, in an attempt to characterize LC's dynamic underlying relationship with arousal.

Here, we modified a squeezing task, previously shown to induce sympathetic arousal and increase norepinephrine activity (Kozłowski et al., 1973; Lake et al., 1976; Mather et al., 2020; Nielsen et al., 2015; Nielsen and Mather, 2015; Vecht et al., 1978; Wallin et al., 1992, 1987) to create a pseudo-resting state fMRI paradigm to up-regulate LC (Hussain et al., 2019; Mather et al., 2020). We then used an HMM to characterize spatial patterns of co-activation among 31 'nodes' comprising four known networks in the brain – the default mode network (DMN), dorsal attention network (DAN), fronto-parietal control network (FPCN), and salience network (SN) (Deshpande et al., 2011; Laird et al., 2005; Lancaster et al., 2007; Raichle, 2011) – as well as the LC itself (Langley et al., 2021, 2020). We then examined the states and their behaviors extracted via the HMM, including spatial patterns of brain activity and dynamics of state occupancy and transitions between states. We also used custom MRI sequences to measure LC neuronal density as a proxy for neuromelanin (Langley et al., 2020, 2017) to examine how individual differences in LC structure affect these measures.

The HMM was able to extract five stable brain states, including a highly stable state we can identify as a state of arousal that occurred when subjects engaged with the squeezing task; the stability of this state was correlated with LC neuronal density. Further, propensity to dwell in this state, as well as the propensity to transition into this state from a state of relative deactivation, were both correlated with LC neuronal density. Together, our results reveal that our handgrip task was effective at changing the ease of transition into an aroused state and the time spent in that state once achieved, and that individual differences in LC neuromelanin explain important individual differences in probability of attaining and maintaining a state of arousal even in healthy young adults.

2. Results and discussion

2.1 Neuromelanin results

We computed LC magnetization transfer contrast (MTC) using neuromelanin MRI (NM-MRI) to quantify LC neuronal density and thus quantity of neuromelanin in this structure (Langley et al., 2020, 2017). Across subjects, the mean (\pm s.d.) LC MTC was 0.1212 ± 0.0220 mm³. These values were correlated with the various model outputs as described in **Methods**.

2.2 Descriptive model outputs

2.2.1 Activation state pattern characterization

Figure 2A shows the activation state patterns recovered by the fitted HMM. State 1 (S1) appears to represent a DMN-dominant state because DMN showed the highest level of activation, while State 2 (S2) corresponds to an attention-dominant state since DAN and SN showed the highest levels of activation. State 3 (S3) shows all networks investigated to be activated, and State 4 (S4) can be labeled as the squeeze/sham state because it was prevalent during the squeeze/sham periods of the paradigm (**Figure 3**). Because this state was also prevalent during the “squeeze” periods of the sham condition, where the subjects lifted their arm to their chest but refrained from squeezing, S4 will be referred to as the arousal state. In keeping with this labeling, S4 also shows a dramatic increase in the activation level of some ROIs in the attention networks, DAN and SN – specifically the right anterior prefrontal cortex and left insula – as well as relative *deactivation* of LC. Finally, all networks were deactivated in State 5 (S5), perhaps because another network not examined in this investigation was activated (e.g., visual networks). Furthermore, we note that many of these states showed qualitative relationships to one another. For example, S1 and S4 visually appear to have similar patterns, but with opposite signs, such that DMN showed high levels of activation in S1 but was deactivated in S4. Conversely, right anterior prefrontal cortex and left insula in SN were deactivated in S1 but were activated in S4.

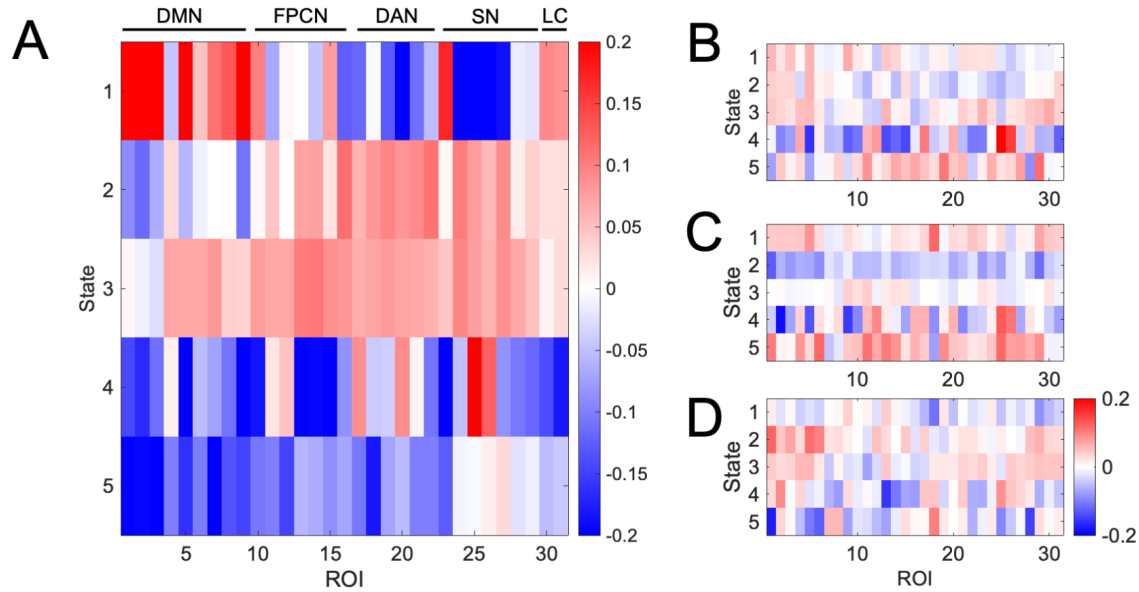


Figure 2. The five stable activation state patterns extracted by the fitted HMM. **(A)** Activation state patterns show interpretable qualitative patterns, such that state 1 (S1) appears to be DMN-dominant, S2 appears SN-dominant, S3 shows broad activation across all networks, S4 appears to reflect an aroused brain state during squeeze periods (see also **Results Section 2.2.2**), and S5 shows broad deactivation across networks. **(B)** and **(C)** show activation state patterns as a function of active versus sham condition, respectively, found by the *Viterbi averaging method* (**Methods Section 3.3.1.1**). Activation state patterns for **(B)** active and **(C)** sham conditions show some qualitative and quantitative similarities (especially in S4), but also display important differences, shown in **(D)** which displays active minus sham. Units are normalized BOLD. See main text for detailed analysis.

To facilitate direct comparison with the active- and sham-specific patterns, we next applied the *Viterbi averaging method* to retrieve the state patterns separated into active versus sham conditions (**Figure 2B** and **2C**, respectively; see **Methods Section 3.3.1.1**), first at the whole group mean level. For mean states across all subjects, state-wise Pearson correlation coefficients between active and sham for S1-S5 and their significance (p-values) are given in **Table 1**.

	Pearson's r	p
State 1	0.3763	0.0369*
State 2	-0.1738	0.3499
State 3	0.2447	0.1846
State 4	0.7887	< 0.001*
State 5	0.1739	0.3494

Table 1. Group-defined states show differences between active and sham conditions, quantified by the (lack of) statistically significant Pearson correlation coefficients (r) between active and sham versions of each state except for two states: S1, the DMN-dominant state, and S4, the arousal state, showed significant correlations between active and sham. * $p < 0.05$.

States 1 and 4, the DMN-dominant state and the arousal state, respectively, show quantitative similarities between conditions, but the others states do not (**Figure 2D**). At the individual level, we repeated this process and correlated active and sham for each subject and each state. All but S4 showed a difference between active and sham conditions. This was revealed by a one-way repeated measures ANOVA with state as a factor, testing the Fisher-z transformed correlation coefficients between active and sham. This ANOVA showed a main effect of state ($F(4,108) = 5.803, p < 0.001$). We followed this with step-down t-tests against 0 to explore which state(s) were significantly correlated across active versus sham condition (**Table 2**).

	Mean Pearson's r	σ	t	p
State 1	0.1770	0.3436	0.1888	0.8594
State 2	0.0086	0.3100	0.0584	0.9571
State 3	-0.0026	0.2998	0.7567	0.4915
State 4	0.2659	0.3360	5.4652	0.0055*
State 5	0.0113	0.3143	-0.7775	0.4803

Table 2. Mean Pearson correlation coefficients (r) and t-test results for comparing states between active and sham conditions on a subject-by-subject basis. S4 showed a high degree of stability (significantly positive Pearson correlation coefficients) between the active and sham condition. All statistical tests were performed after the correlation coefficients were Fisher z transformed, but the means and standard deviations are presented in raw correlation coefficient units. * $p < 0.05$

Of the five t-tests against 0, only S4, the arousal state, reached significance. These tests demonstrate that there are likely significant variations in the state patterns between active versus sham conditions, but S4 remained highly stable across this manipulation even at the individual subject level. Although this may seem surprising given that the experimental manipulation was at its 'largest' during the squeeze periods (subjects either squeezed or held the ball to their chest), further scrutiny suggests that the downstream effects on the other networks are expected to exhibit the most variation as a function of the experimental squeeze manipulation. That is, because of the difficulties in measuring LC activity or connectivity directly, we should expect to see differences in states as a function of condition not precisely at the point of LC up-regulation, but in downstream effects on network activation patterns throughout the subsequent resting-state periods of the scan. Thus, going forward, we can see that S4 is indeed a stable, arousal state that makes a strong anchor point to focus the remaining analyses.

We can also characterize the differences between active and sham in the state patterns themselves. S1 (DMN-dominant) displays higher activity levels in the sham than the active condition, while the opposite is true for S2 (attention-dominant). That S2 has higher activity in the active than sham condition suggests that LC activation in the active condition may have increased attention and arousal; this is also consistent with the observation that S3 (all networks activated) shows higher activity in active than sham, while the opposite is true for S5 (all networks deactivated). And even visually, one can see that the smallest differences between active and sham appear to occur in S4, consistent with the statistical analysis above.

Finally, we calculated the Euclidean distance between active and sham conditions for each state and each subject, and then correlated these distances with LC MTC to determine whether LC MTC moderated the effects of the active squeeze manipulation. We found that only S4 showed a trending relationship with LC MTC (**Table 3**), but importantly that this trending relationship was an inverse relationship: higher LC MTC was associated with smaller distance (i.e., greater degree of similarity) between the active and sham condition instantiations of this state. This finding suggests that LC neuromelanin is involved with stabilizing this state of arousal, and that individual differences in LC MTC even in younger adults can exert significant effect on arousal states of neural activity.

	Spearman's r	p
State 1	-0.0482	0.8075
State 2	-0.0757	0.7066
State 3	0.0077	0.9700
State 4	-0.3629	0.0584 [†]
State 5	0.1910	0.3287

Table 3. Spearman correlation coefficients between LC MTC and the Euclidean distance separating state activation patterns during active and sham conditions as a function of state. S4 showed a trending anti-correlation between LC MTC and distance, i.e. that higher LC neuromelanin was associated with smaller distance between active and sham conditions for the activity pattern associated with this state. [†] $p < 0.1$

2.2.2 Viterbi path

The Viterbi paths for active and sham conditions are illustrated in **Figure 3**. Remarkably, the squeeze periods within the *post-arousal* (PostAr) block (after the first squeeze or hand-raise had occurred; see **Methods Section 3.1.1.2**) were obvious, as almost all subjects visit S4 (the orange state) in both active and sham conditions for almost the entire length of the PostAr blocks at time points 151-159, 220-228, 289-297, 448-456, and 487-495 – visible as vertical orange bars running through almost all subjects.

Visually, we see hints that the Viterbi paths may be different between active and sham conditions. For example, S3 seems more prominent in active than sham, whereas S1 may be more prominent in sham. S5 also appears to occur more often in sham. Rather than rely on visual inspection, we quantitatively compared the behavior and dynamics of the active and sham Viterbi paths and describe the results in the next sections.

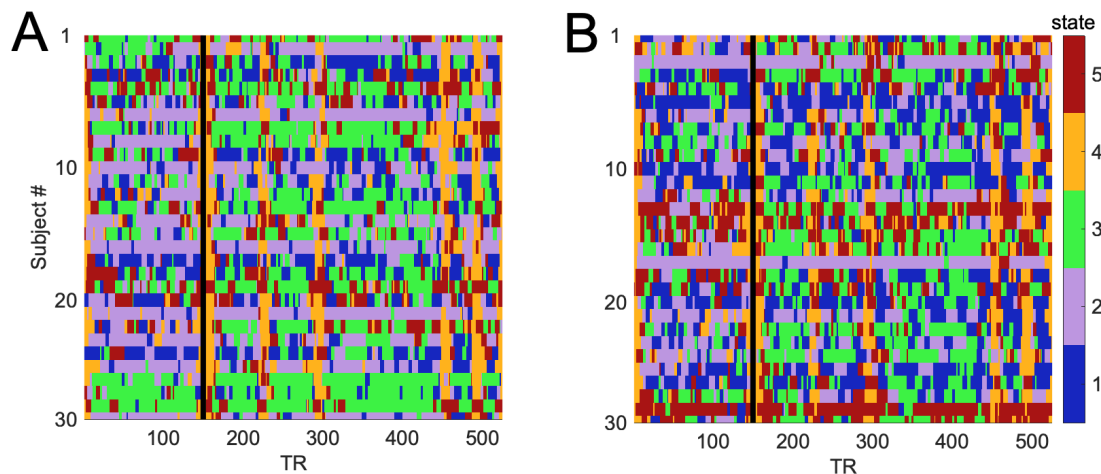


Figure 3. Viterbi paths for active and sham conditions. Visually, there appear to be meaningful differences in the state trajectories between active (**A**) and sham (**B**) conditions; these differences are quantitatively tested in the next sections. Vertical black lines indicate the break between RS0 (before any squeezing or hand-raising) and PostAr (after the first squeeze/hand raise) blocks (see **Methods Section 3.1.1.2**).

2.3 Brain state behavior & covariance with LC structure

We next examined several dynamic aspects of the state space trajectories themselves (see **Methods Section 3.3.2**). These measures were also correlated with LC MTC. See **Methods** for details.

2.3.1 Average state duration

The first behavior we examined were the baseline-corrected average state durations (**Methods Section 3.3.2.1**). An omnibus 2 (condition: active vs sham) x 5 (state) ANOVA showed a main effect of state ($F(4, 116) = 11.155, p < .001$) but no main effect of condition ($F(1, 116) = .355, p = .556$) and no interaction ($F(4, 116) = .231, p = .921$) (**Figure 4A**). This pattern suggests that once subjects entered a state, the amount of time they dwelled in that state differed from one state to the next but did not differ across the active versus sham manipulation. We therefore collapsed across conditions and recalculated average state duration on the collapsed dataset, and followed this with a one-way repeated measures ANOVA testing for a main effect of state on duration.

This process revealed a main effect of state ($F(4, 116) = 7.236, p < .001$), which we then followed with five t-tests against 0 to see which states had higher or lower average duration in the PostAr block relative to baseline (RS0, before any squeezing or hand-raising had occurred; see **Methods Section 3.1.1.2**). These tests revealed that three states were on average significantly longer or shorter in duration in PostAr than in RS0 (**Table 4**): S3 (“everything is activated”) and S4 (arousal state) were significantly longer in PostAr than in RS0, while S2 (attention-dominant state) was – perhaps surprisingly – significantly shorter in PostAr than in RS0. S2 being longer in RS0 than PostAr may make sense because RS0 occurred at the beginning of a relatively long scan session, so subjects may have been alerted by the sounds of

the scanner or instructions from the experimenter. S3 being longer in PostAr may similarly be related to the short duration of RS0, as well as the relatively less time spent in this state (see **Results Section 2.3.3**, below). S4 being longer in PostAr makes sense also because this is where the squeeze periods occurred, and so S4 rarely occurred during RS0 and only at the very beginning of this first scan run (**Figure 3**) and therefore its duration was truncated.

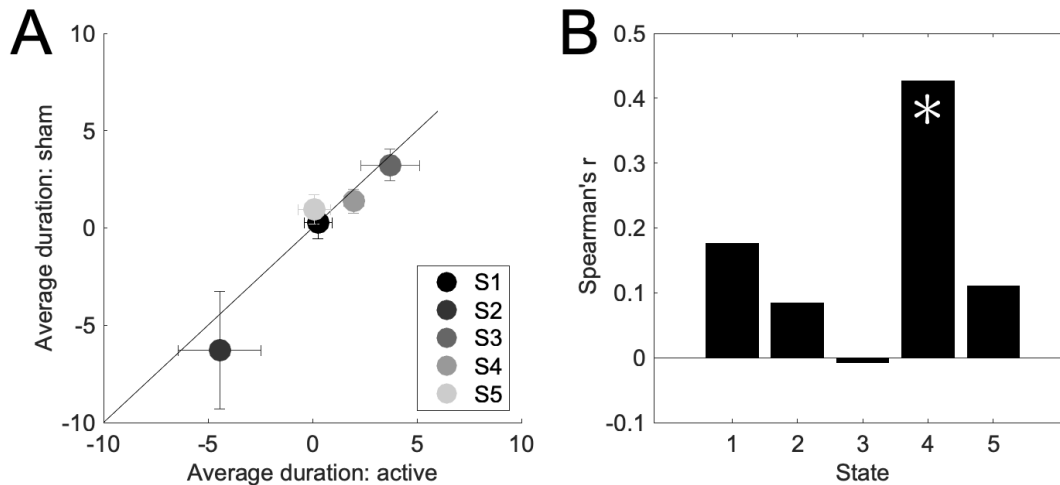


Figure 4. Average baseline-corrected state durations (ΔDur) in the active and sham conditions, and correlations with LC MTC across subjects. **(A)** The 2 (condition: active vs sham) x 5 (state) repeated measures ANOVA revealed no main effect of condition but a main effect of state, which is visible in the nearness of the points to the identity line. **(B)** Average durations for S4, the arousal state, showed significant ($p = 0.0246$) correlation with LC MTC: the more neuromelanin present in a subject's LC, the longer the participant tended to dwell in S4 (after correcting for baseline). No other correlations with LC MTC reached significance. Error bars in **(A)** show the standard error of the mean. See main text for details. * $p < 0.05$

	Mean ΔDur (PostAr-RS0)	σ	t	p
State 1	0.1695	2.5420	0.3652	0.7176
State 2	-2.4595	5.5043	-2.4595	0.0201*
State 3	2.1018	3.7688	3.0545	0.0048*
State 4	1.2557	2.5320	2.7163	0.0110*
State 5	-0.3500	2.6876	-0.7133	0.4814

Table 4. Average changes in durations and t-test results for comparing state duration changes relative to baseline across state, collapsed across conditions. Three states (S2, S3, and S4) showed significantly different durations in PostAr relative to baseline (RS0): S2 showed significantly shorter durations in PostAr, while S3 and S4 showed significantly longer durations in PostAr. See main text for details. * $p < 0.05$

Finally, we also wanted to see whether LC neuromelanin could predict changes in state duration from baseline, across subjects. To answer this question, LC MTC was correlated with the average duration of all five states after (**Figure 4B**) collapsing the data across conditions as above since this factor was nonsignificant in the omnibus ANOVA. The Spearman's r values in **Figure 4B** were acquired by correlating LC MTC with the difference in average duration across baseline, i.e. $\text{corr}(\Delta\text{Dur}, \text{LC MTC})$ (concatenated across conditions).

Here, we observed only one significant correlation between LC MTC and the average duration of S4 (arousal state) (**Table 5**). This is particularly noteworthy as S4 occurs in both active and sham conditions as a direct consequence of the task manipulation, and reflects engagement with a cognitive and motor task. That is, this result shows that the amount of neuromelanin in a subject's LC impacts how long that subject persists in the arousal state, regardless of the active versus sham condition manipulation: the higher the inferred neuronal density in a given subject's LC, the longer they persist in an arousal state once they achieve it. We noted in our first characterization of S4 (**Results Section 2.2.1**) that S4 contains targeted increases in activity in two nodes in particular, the right anterior prefrontal cortex and left insula, and relative deactivation of LC. Nevertheless, we can see that LC structure significantly predicts how long the aroused state persists once it is achieved. As we will see in the next sections, this focus on S4 as being especially sensitive to task demands and LC MTC is maintained through the next analyses.

	Spearman's r	p
State 1	0.1762	0.3680
State 2	0.0837	0.6708
State 3	-0.0077	0.9700
State 4	0.4264	0.0246*
State 5	0.1100	0.5773

Table 5. Spearman correlation coefficients (r) comparing LC MTC to average state duration change from baseline, collapsed across conditions. The change in duration (relative to baseline) of S4, once entered into, was significantly correlated with LC MTC across subjects. See main text for details. * $p < 0.05$

2.3.2 Transition probabilities

Next, we asked whether transition behavior between pairs of states was modulated by our active versus sham condition manipulation, and how these changes might be related to LC neuromelanin. This analysis involves computing the transition probability matrices (TPMs), relative transition probability matrices (RTPMs), and their differences as a function of condition (see **Methods Section 3.3.2.2** for details).

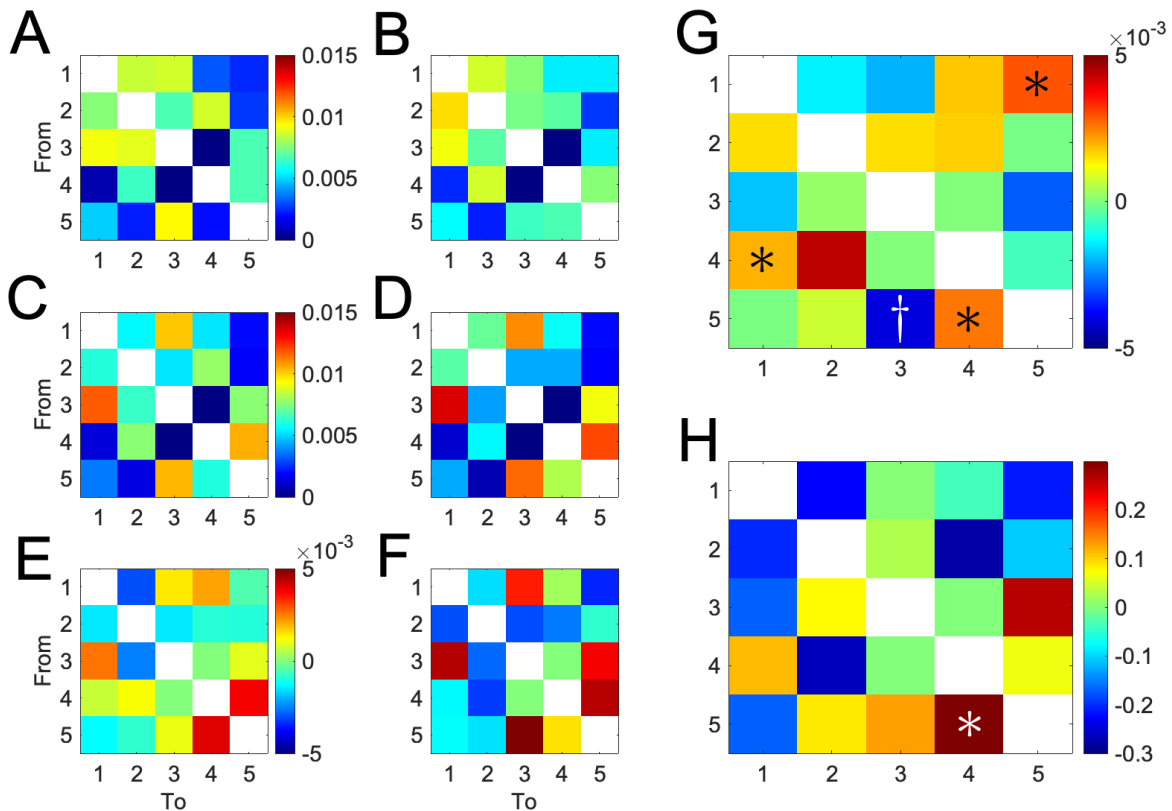


Figure 5. Transition probability matrices (TPMs), relative transition probability matrices (RTPMs), and correlations with LC MTC. Each colored square in (A)-(F) shows the transition probability from state i to state j , with i represented by rows and j represented by columns. (A) and (B) display the TPMs for RS0 in the active and sham conditions, respectively. (C) and (D) show the TPMs for PostAr for active and sham conditions, respectively. (E) and (F) show the RTPMs for active and sham conditions, i.e. the differences between TPMs for PostAr and RS0 ((E) = (C) - (A) and (F) = (D) - (B)). (G) shows that several of the differences in transition probability from baseline were significantly larger in the active than the sham condition ($S4 \rightarrow S1$, $S5 \rightarrow S4$, and $S1 \rightarrow S5$; (G) = (E) - (F), Wilcoxon sign rank test against 0), while one difference in transition probability from baseline was trending smaller ($S5 \rightarrow S3$). Finally, (H) shows the Spearman correlation coefficients relating values shown in (F) and LC MTC across subjects; one relative transition probability ($S5 \rightarrow S4$) reached significance. See main text for details. * $p < 0.05$; † $p < 0.1$

First, we can visually examine the average TPMs from RS0 and PostAr, in the active and sham conditions (Figure 5A-D). Visually, we can see reasonable covariation among all of these, suggesting that the pairwise transition behaviors are relatively stable across all blocks and conditions. Recall, however, that RS0 occurred on different days for both active and sham conditions. Therefore, to remove baseline effects, we really want to examine the RTPMs, not the TPMs. RTPMs are defined as the difference in TPM between PostAr and RS0, i.e. how much the TPM changes as a result of the introduction of the squeezing (active) or hand-raising (sham) task relative to baseline transition probabilities occurring during the first resting state period

(RS0). In this case, baseline was important to consider because one subject (or even one condition's RS0 in one subject, given that active and sham were collected on different days; see **Methods Section 3.1.1**) may intrinsically have had a higher switching rate than another subject or condition's RS0. To understand how the handgrip task affected the transition probabilities, we thus removed any baseline effects and corrected for individual differences across subjects by computing the RTPMs. **Panels E and F of Figure 5** show the mean RTPM results for active and sham conditions, respectively.

To address how these transition probabilities relative to baseline changed as a function of active squeeze, we examined the Euclidean distance between these RTPMs for each subject ($\text{RTPM}_{\text{Active}} - \text{RTPM}_{\text{Sham}}$, **Figure 5G**; see **Methods Section 3.3.2.2**). This process identified that on the whole, the distances between $\text{RTPM}_{\text{Active}}$ and $\text{RTPM}_{\text{Sham}}$ were significantly different from 0 across subjects (Wilcoxon sign rank, Mann-Whitney U = 465, $p = 1.7344e-06$), indicating that the change in transition probabilities from RS0 to PostAr was different overall in active versus sham conditions. In other words, the transition probabilities revealed differences between active and sham that were obscured by the average state duration analysis described above.

However, the significant difference in overall RTPMs between active and sham does not account for the transitions between specific states. To test whether state-specific changes in transition probabilities from baseline were different between active and sham conditions, we conducted separate Wilcoxon sign rank tests for each state in the off-diagonal transition probabilities in $\text{RTPM}_{\text{Active}} - \text{RTPM}_{\text{Sham}}$; that is, for all off-diagonal transition probabilities going from state j to state k , we computed the difference, $\text{RTPM}_{\text{Active},i,j,k} - \text{RTPM}_{\text{Sham},i,j,k}$ ($i \in \{\text{subjects}\}$) and then tested whether the distribution of these differences across subjects was significantly different from 0 for every pairwise state transition using a Wilcoxon sign rank test. Now, we can see which pairwise state transitions are likely to be driving the overall differences between active and sham RTPMs. Several states showed significant differences between $\text{RTPM}_{\text{Active}}$ and $\text{RTPM}_{\text{Sham}}$ that were specific to certain state transition probabilities, summarized in **Figure 5F**.

Let us first focus on transitions into and out of S4, as that is the arousal state which we found to have duration significantly correlated with LC MTC regardless of active versus sham condition (**Results Section 2.3.1**). In the RTPM differences ($\text{RTPM}_{\text{Active}} - \text{RTPM}_{\text{Sham}}$, **Figure 5G**), we now see that two transitions that involve S4 were significantly different between active and sham conditions after correcting for baseline effects. Namely, $S4 \rightarrow S1$ ($p = 0.0467$) and $S5 \rightarrow S4$ ($p = 0.0226$) were both significantly more likely to occur in the active than the sham condition. This observation can be interpreted as when subjects actively squeezed, they were more likely to go from a relatively deactivated state (S5) to an arousal state (S4) than when they simply brought their hand to their chest, and likewise that once they achieved that arousal state (S4) they were more likely to transition into a DMN-dominant state (S1) in the active than in the sham condition. This suggests not only that the squeeze manipulation was successful in easing the transition into an arousal state (Hussain et al., 2019; Kozłowski et al., 1973; Lake et al., 1976; Mather et al., 2020; Nielsen et al., 2015; Nielsen and Mather, 2015; Wallin et al., 1992, 1987), but also that once the arousal state was achieved, subjects more easily transitioned into an internally-oriented mental state (DMN is associated with internally-oriented attention and self-referential mind wandering (Raichle, 2015, 2011)) than in the sham condition.

This pattern might seem counterintuitive, as one might expect an attentional state (e.g. S2) being the more likely transition after arousal. One possible explanation is that NE depletion played a role, in that the arousing stressor (squeezing) depleted the LC's supply of NE causing subjects to return to the DMN-dominant state rather than switching into an attention-dominant state (i.e., S2), thereby prompting an attention "reset" (Mather et al., 2016; Sara, 2016, 2015)

rather than a direct transition into S2. Moreover, recall that, aside from the squeeze/hand-raising task, there was no other task for the subjects to do in the scanner; therefore, after entering the arousal state in the active condition, when it started to dissipate they may have had nothing external to focus on and therefore focused on their own thoughts more than in the sham condition. This interpretation is consistent with the observation that the S1→S5 transition was also significantly more likely to occur in active than in sham after correcting for baseline effects ($p = 0.0168$). Interestingly, this suggests the presence of a circular S1→S5→S4→S1 loop that is more likely to occur in active than in sham, but which is broken by the (trending; $p = 0.0937$) stronger presence of S5→S3 in the sham condition (recall that S3 is a more general “everything is active” state rather than the internally-focused S1 or the externally-focused S2). Recall that negative values in **Figure 5G** indicate instances where the change in transition probability relative to baseline was lower during the active condition than in the active condition. Thus, the trending negative value of S5→S3 occurred because the active squeeze impeded an increase in this transition probability relative to baseline, rather than the active squeeze having no or a reduction effect on this probability. This suggests a difference in LC activity between the active squeeze versus the sham (bring arm to chest) control: While lifting the arm to the chest may marginally up-regulate LC activity and induce some arousal (Hussain et al., 2019), there is also a relatively high probability of transitioning between whole-brain activation and whole-brain deactivation states in pure resting state (i.e., no actual task) paradigms (Chen et al., 2016). These results are consistent with previous findings showing common back and forth transitions between whole-brain activation states and whole-brain deactivation states in the absence of a task (Chen et al., 2016). It is possible that the transition S5→S3 was trending significant but S3→S5 was not because slight changes in LC activity led to increased probability to transition out of a whole-brain deactivation state (S5) and into a whole-brain activation state (S3) where attentional networks were activated, rather than the other way around (Hussain et al., 2019).

Although we can only speculate here as to why this S1→S5→S4→S1 loop was more likely to occur in active than in sham, it appears that the increased arousal due to the active squeeze may have kept participants more engaged throughout the scan, even if that engagement was oriented inwards. It is of course also possible that subjects transitioning out of the DMN-dominant state and into the whole-brain deactivation state could indicate that a network not analyzed in this study is at work in response to the active squeeze; we leave exploration of this possibility to future studies.

Interestingly, no subject experienced S3→S4 or S4→S3 transitions in either the active or sham condition (darkest blue squares in **Figure 5A-D**). To understand the significance of this observation, recall that S3 is the “everything is activated” state and S4 is the arousal state. One possible explanation for this observation is that LC could be involved in allocating attention (Sara, 2015). Previous studies have shown that an increase in LC activity may cause a rapid shift in allocation of attention in response to the sudden onset of a stimulus (Sara, 2016, 2015). This may be why subjects did not transition from the arousal state (S4) into the whole-brain activation state (S3) where all attention-related networks were concurrently activated, and the LC induced some phenomenon that could not be observed in this investigation. Instead transitions from S4 into S1, S2, or S5 were seen where DMN, FPCN, DAN, and SN were not synchronously activated – only a few (two at most as seen in S2) were activated at the same time. The LC allocated attention to DAN and SN since the subjects were observed to transition out of S4 into S2. Attention was also allocated to a resting state network (DMN in S1) since some subjects returned to resting state following the squeeze periods. Some attention could have been allocated to a network not examined (S5), albeit more so in the sham condition than in the active, but never to DMN, FPCN, DAN, and SN at the same time. Because this idea of attentional allocation is associated with network resetting, our results may provide preliminary

evidence that HMM-derived states can test the LC network reset hypothesis (Sara, 2016, 2015). However, additional tests focusing on attentional shift during these specific transitions are needed.

Finally, we were interested in how LC neuromelanin levels were related to changes in transition probabilities from RS0 to PostAr, especially given the observation that LC MTC significantly correlated with S4 duration in the previous analysis. To answer this question, LC MTC values were correlated with $RTPM_{Active} - RTPM_{Sham}$ across all subjects prior to obtaining the global average (**Figure 5G**). Once again, we saw significant correlations having to do with S4, the arousal state. A significant correlation was observed between LC MTC and the changes in the S5→S4 transition from baseline ($p = 0.0150$), indicating that LC neuromelanin levels may mediate the probability of subjects transitioning out of the whole-brain deactivation state and into the arousal state as a function of the handgrip task relative to baseline.

Together, these results paint a compelling picture. LC MTC appears to moderate the persistence of an arousal state (S4) once entered, regardless of how the subject ended up in the state, as well as the propensity to transition into that state especially from positions of relative overall deactivation. However, one potential confounding factor is that LC MTC might simply correlate with the predominance of S4 in general: If S4 is more likely to occur in subjects with higher neuronal density in LC regardless of task or previous state, that could offer a less exciting explanation for why we have seen the patterns described here. We sought to rule out this possibility by conducting the fractional occupancy analyses described next.

2.3.3 Fractional occupancy

To determine whether the results above may be trivially due to differences in fractional occupancy in S4 (or other states) across active and sham conditions, or differences in LC MTC that drove such a propensity to occupy S4, we directly examined the percent of time each subject spent in each state. That is, we calculated the fractional occupancy (**Methods Section 3.3.2.3**) for each state and within each block (RS0 vs PostAr), and then performed analyses similar to those done above for average state duration on the difference between these, ΔFO .

The 2 (condition: active vs sham) x 5 (state) repeated measures ANOVA revealed a main effect of state ($F(4,100) = 14.51$, $p < .001$) and a trending main effect of condition ($F(1,100) = 3.90$, $p = 0.059$), but no interaction ($F(4,100) = 1.73$, $p = 0.150$) (**Figure 6A**). We thus collapsed across conditions and conducted a one-way repeated measures ANOVA to evaluate whether state affected fractional occupancy regardless of active versus sham condition. This approach revealed a main effect of state ($F(4,116) = 14.27$, $p < .001$), so we followed these findings with five t-tests against 0 to discover which states deviated in their fractional occupancy between RS0 and PostAr. These tests revealed that subjects spent a significantly higher percentage of their time in S2 during the PostAr block versus RS0, but significantly lower percentage of the time in S3 and S4 (**Table 6**). While these may seem surprising, recall that fractional occupancy is defined as the percentage of time spent in a particular state relative to the total length of the scan, and the RS0 block is only 150 TRs long while the PostAr block is 375. Thus, any occupancy in short-lived states like S4 (see **Results Section 2.3.1**) during RS0 might lead to a relatively outsized appearance of fractional occupancy.

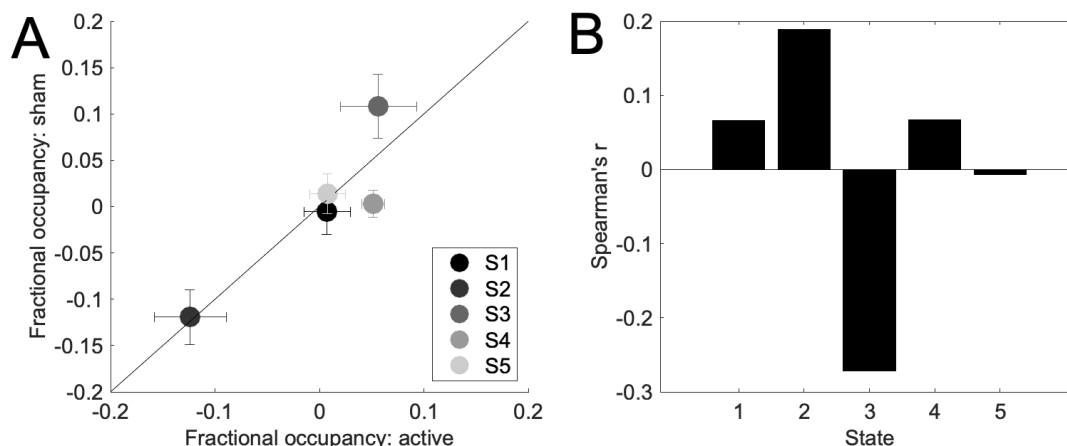


Figure 6. Average baseline-corrected fractional occupancy (ΔFO) in the active and sham conditions, and correlations with LC MTC across subjects. **(A)** The 2 (condition: active vs sham) \times 5 (state) repeated measures ANOVA revealed no main effect of condition but a main effect of state, which is visible in the nearness of the points to the identity line. **(B)** No state's fractional occupancy significantly correlated with LC MTC. Error bars in **(A)** show the standard error of the mean. See main text for details.

	Mean ΔFO (PostAr-RS0)	σ	t	p
State 1	-0.0009	0.0937	-0.0506	0.960
State 2	0.1215	0.1103	6.0354	< .001*
State 3	-0.0825	0.1262	-3.5827	0.001*
State 4	-0.0273	0.0511	-2.9240	0.007*
State 5	-0.0108	0.0878	-0.6754	0.505

Table 6. Average fractional occupancy and t-test results for comparing fractional occupancy changes from baseline across state, collapsed across condition. Three states (S2, S3, and S4) showed significant differences in fractional occupancy during PostAr relative to baseline (RS0): S2 was occupied significantly more often in PostAr, while S3 and S4 were occupied significantly less often relative to the length of the block. See main text for details. * $p < 0.05$

Nevertheless, our goal with this analysis was to identify a potential origin for the aforementioned result demonstrating that average duration of S4, or transition into S4 or other states, was related to LC MTC. Thus, as a final check we correlated ΔFO with LC MTC across subjects. This analysis revealed no significant correlations between the fractional occupancy in any state and LC MTC (**Figure 6B**; **Table 7**). We can therefore be confident that the relative higher probability of transitioning S5→S4 in the active condition, and the observed correlation between this specific transition and LC MTC across subjects, is unlikely to be attributed to percent of time

spent in S4 or any effect of LC MTC on this fractional occupancy. Instead, it seems likely that the S5→S4 transition as well as the duration of S4 – and their correlations with LC MTC – reflect a core role of LC neuronal density on the effectiveness of the active squeeze manipulation on the ease of entering into an aroused state.

	Spearman's r	p
State 1	0.0662	0.7371
State 2	0.1894	0.3344
State 3	-0.2715	0.1619
State 4	0.0673	0.7335
State 5	-0.0071	0.9722

Table 7. Spearman correlation coefficients comparing LC MTC to ΔFO (average fractional occupancy change from baseline), collapsed across conditions. No changes in fractional occupancy were significantly correlated with LC MTC. See main text for details.

2.4 Summary, limitations, & conclusions

Here, we sought to characterize the consequences of LC up-regulation on the spatiotemporal dynamics of brain networks. We fitted a hidden Markov model (HMM) to whole-brain fMRI data while healthy adult humans performed a pseudo-resting-state task designed to engage LC, and examined how LC activation modulated brain states themselves as well as the dynamics of transitions between them. The HMM identified five stable states corresponding to patterns of activity in the default mode network (DMN), dorsal attention network (DAN), front-parietal control network (FPCN), salience network (SN), and the LC. One of these states, the 'arousal' state – which occurred during active engagement with the squeezing task (during both active and sham conditions) – was highly stable across conditions, although other states showed significant difference between active and sham. Interestingly, the stability of this arousal state, S4, was correlated with LC neuromelanin (LC MTC). Further, the degree to which the squeeze task affected subjects' propensity to transit into S4 was also correlated with LC neuromelanin (LC MTC), and LC MTC also showed correlations with the duration of that state once it was achieved, regardless of active versus sham condition. We interpret these results to mean that, even in healthy young adults, LC structure plays an important role in facilitating the transition into an arousal state, moderating the efficacy of any task or condition that might engage the LC circuit to cause norepinephrine release.

These findings can be applied in future studies to better characterize previous observations that LC activation contributes to not just an aroused state but also a U-shaped function relating arousal and performance, known as the Yerkes-Dodson curve (Aston-Jones and Cohen, 2005). Our data-driven approach, using a HMM to reveal hidden states of network activity patterns, clearly identified an arousal state in S4 which was highly stable even in the absence of an active stress-type manipulation (the squeeze), but which nevertheless showed meaningful hallmarks both of our behavioral manipulation and of individual differences in neuromelanin. In particular,

under the active squeeze condition, network nodes in SN exhibited stronger activation and subjects tended to persist longer in this state when they actively squeezed, depending on their LC neuromelanin level. Notably, these results demonstrate that network-based approaches to studying the effects of LC up-regulation can identify meaningful patterns even in the absence of precise measurement of LC activity itself. That the squeeze manipulation also eased the transition into this arousal state from a state of relative deactivation is not only consistent with previous findings showing that arousal may be more easily achieved if LC is successfully engaged (Hussain et al., 2019; Kozłowski et al., 1973; Lake et al., 1976; Mather et al., 2020; Nielsen et al., 2015; Nielsen and Mather, 2015; Wallin et al., 1992, 1987), but also allow us to examine what that state of arousal consists of: relative deactivation of nearly every other network in the brain studied here with the exception of two nodes in FPCN (left and right posterior inferior parietal lobule) and two nodes in DAN (left anterior prefrontal cortex and left anterior insula). In contrast, DMN was almost entirely deactivated in this arousal state, in stark contrast to its high degree of activation that likely occurred directly after presence in the arousal state (in the DMN-dominant state, S1). Moreover, that the S4→S1 transition was more likely in the active than sham condition – and that the subsequent S1→S5 transition was also more likely – suggests a cycle of outward orientation (S4) followed by relatively inward-directed attention (S1) and then a general resetting (S5) that is significantly driven by LC activity levels. Future research may more explicitly explore these cycles and include more brain networks to more fully characterize recurring patterns of transitions through state space and their relationship to LC activity and neuromelanin content, as well as using this approach to study the extreme ends of the U-shaped Yerkes-Dodson curve (Aston-Jones and Cohen, 2005).

Although robust across several metrics, the effects we found here were relatively small in size. This may have occurred because the handgrip manipulation was not strong enough to induce changes in LC activation (and consequences in brain states and dynamics) large enough to be detected via fMRI. Future studies may wish to employ a more aggressive manipulation, such as subjects dipping their hand in cold water, administering electrical pulses, or presenting jarring sounds (Marmon and Enoka, 2010; Oyarzún et al., 2012; Redondo et al., 2008; Schwabe and Schächinger, 2018; Stark et al., 2006). It is also possible that we would see stronger results in older adults or in a diseased population (i.e., subjects with Parkinson's or Alzheimer's diseases), as neuromelanin accrues with age and peaks between ages 50-60 (Manaye et al., 1995; Ma et al., 1999; Zecca et al., 2004). Nevertheless, we did observe reasonable variation in LC neuromelanin across subjects even in this young, healthy population, contributing to knowledge of individual differences in LC structure and function.

On the other hand, if the squeeze manipulation we used did in fact induce a robust LC response and consequences in brain dynamics, it is also possible that the measures used in this investigation were not sensitive enough to detect it due to poor signal-to-noise ratio in the BOLD signal. Future investigations could explore various denoising methods for BOLD data (Kundu et al., 2012; Quian Quiroga and Garcia, 2003). As mentioned above, LC BOLD is subject to physiological noise, specifically cardiac pulsation and respiration (Clewett et al., 2016; Glover et al., 2000; Liu et al., 2017; Mather et al., 2017). Here, we were unfortunately unable to regress out these potential noise sources because physiological data were not collected in conjunction with functional data. Future studies should plan to collect cardiac pulsation and respiration data so that physiological noise can be regressed out from the LC BOLD signal prior to HMM fitting (Glover et al., 2000).

Overall, we have shown that individual differences in LC neuromelanin – even in healthy young adults – impact the stability of an arousal-related brain state, and the propensity to enter and

dwell in this state. Our results reveal important new insight into the role of LC in directing the dynamics of brain states related to arousal and task engagement.

3. Methods

In this section we first explain the experimental paradigm and neuroimaging data collection and analysis for both structural and functional data, including measures of LC neuronal density. We also introduce four attention-related networks and describe the HMM to be fitted. The next sections then describe how we approached answering questions about how activation of LC through the behavioral task affects brain network activity and state dynamics. This includes analyzing the HMM-derived brain states themselves as well as their behavior through time. In the supplemental material (**Supplementary Material Section S3.1**), we present methods for collecting and analyzing concurrent pupillometry data, as well as results of that analysis.

3.1 Datasets and Networks

3.1.1 Experimental paradigm and neuroimaging data

3.1.1.1 Participants

Thirty-one healthy human participants (18 females, mean age 25 years \pm 4 years) enrolled in this study at the University of California, Riverside Center for Advanced Neuroimaging. All subjects gave written informed consent and received monetary compensation for their participation. All procedures were approved by the University of California, Riverside Institutional Review Board.

3.1.1.2 Paradigm

The experimental paradigm is illustrated in **Figure 7**. All subjects first underwent a five-minute pure resting state block (RS0) prior to any squeeze. Following this RS0 block, subjects underwent a 12.8-minute experiment where they alternated between resting state and bringing their dominant hand to their chest to squeeze a squeeze-ball at maximum grip strength (SQ1-RS5) (Hussain et al., 2019; Mather et al., 2020). All five squeeze periods lasted 18 seconds while the interspersed five resting state periods had durations of two-, two-, five-, one-, and one-minute, respectively. SQ1 through RS5 occurred after the arousing stressor has been introduced, so we refer to them collectively as the post-arousal (PostAr) block. RS0 and PostAr blocks were collected separately within each condition, for a total of four runs of functional data collection. In order to create a within-subject experimental design, all subjects underwent two sessions corresponding to two different conditions: one where they executed the squeeze (active condition), and one where they still brought their arm up to their chest but were instructed simply to hold the ball and not to squeeze it (sham condition). Condition order was pseudorandomly counterbalanced across subjects, and each condition occurred on a separate day. Following this resting state paradigm, subjects took part in an auditory oddball detection task, the details of which have been described elsewhere but which are not analyzed in the present project (Yaghoubi et al., 2019).

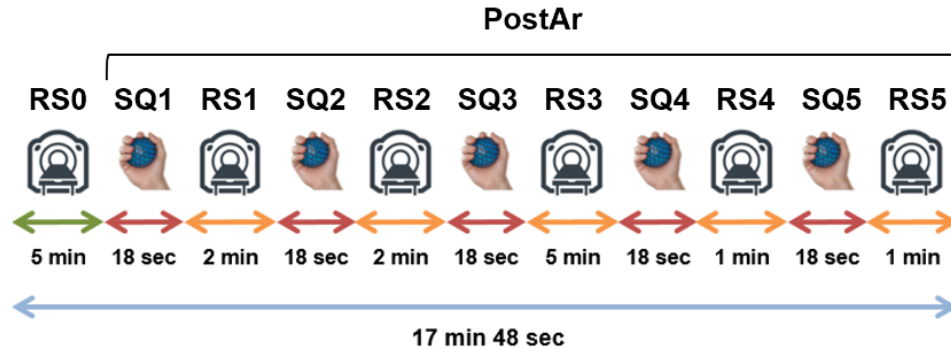


Figure 7. Experimental paradigm consisting of a pure resting state block and a longer alternating squeeze/resting state block to facilitate dynamic (time-varying) analysis (Nielsen and Mather, 2015). Subjects underwent two conditions: (1) an *active* squeeze condition, in which they lifted their arm to their chest and squeezed a squeeze-ball at maximum grip strength for the duration of each squeeze period; and (2) a *sham* control condition, in which they also lifted their arm to their chest during these periods but refrained from squeezing. Within the post-arousal (PostAr) block, RS refers to resting state periods, and SQ to periods in which subjects lifted their arm to their chest and either squeezed (active condition) or did not squeeze (sham condition). The RS0 blocks were used as a baseline for each condition.

3.1.1.3 Functional and structural neuroimaging data acquisition and preprocessing

Magnetic resonance imaging (MRI) data were collected on a Siemens 3T Prisma MRI scanner (Prisma, Siemens Healthineers, Malvern, PA) with a 64 channel receive-only head coil. fMRI data were collected using a 2D echo planar imaging sequence (echo time (TE) = 32 ms, repetition time (TR) = 2000 ms, flip angle = 77°, and voxel size = 2x2x3 mm³, slices=52) while pupillometry data (see **Supplementary Material Section S3**) were collected concurrently with a TrackPixx system (VPixx, Montreal, Canada). Anatomic images were collected using an MP-RAGE sequence (TE/TE/inversion time = 3.02/2600/800 ms, flip angle = 8°, voxel size = 0.8x0.8x0.8 mm³) and used for registration from subject space to common space. One subject was excluded due to a history of attention deficit hyperactive disorder and consumption of related medication, such that the final dataset contained n = 30 subjects (Hussain et al., 2019; Yaghoubi et al., 2019).

The functional data underwent a standard preprocessing pipeline in the functional magnetic resonance imaging of the brain software library (FSL): slice time correction, motion correction, susceptibility distortion correction, and spatial smoothing with a full width half maximum value of 2mm (Smith et al., 2004; Woolrich et al., 2009). Finally, all data were transformed from individual subject space to Montreal Neurological Institute (MNI) standard space using the following procedure in FSL (Smith et al., 2004; Woolrich et al., 2009). First, the T₁-weighted image was skull stripped using the brain extraction tool. Next, brain extracted T₁-weighted images were aligned with the MNI brain extracted image using an affine transformation. Finally, a nonlinear transformation (FNIRT) was used to generate a transformation from individual T₁-weighted images to T₁-weighted MNI common space (Smith et al., 2004; Woolrich et al., 2009).

3.1.1.4 Regions of interest: attention-related networks

To examine the impact of LC up-regulation on network states and dynamics, we selected four networks often associated with resting state: default mode network (DMN), fronto-parietal control network (FPCN), dorsal attention network (DAN), and salience network (SN). DMN (a resting state network) and DAN (an attention network) were selected because squeezing ought to invoke a transition from the resting state into a task-positive state (Greicius and Menon, 2004); FPCN because it is linked to DAN and regulates perceptual attention (Dixon et al., 2018); and SN because it determines which stimuli in our environment are most deserving of attention (Mather et al., 2020; Menon and Uddin, 2010). Talairach coordinates for regions of interest (ROIs) within DMN, FPCN, and DAN were taken from Deshpande and colleagues (Deshpande et al., 2011) and converted to MNI coordinates while SN MNI coordinates were taken directly from Raichle's 2011 paper (Deshpande et al., 2011; Laird et al., 2005; Lancaster et al., 2007; Raichle, 2011). Two ROIs from FPCN (dorsal anterior cingulate cortex and left dorsolateral prefrontal cortex) were excluded due to their close location to other ROIs.

The fifth 'network' we included in fitting the HMM was the bilateral LC itself. LC was localized using the probabilistic atlas described in Langley et al. 2020 (Langley et al., 2021, 2020). Briefly, a reference region was drawn in the pons and its mean (μ_{ref}) and standard deviation (σ_{ref}) were calculated. Next, the LC atlas was transformed from MNI space to native NM-MRI space using procedures outlined in **Methods Section 3.1.1.3** using a threshold level of 0.01. After binarizing and dilating the transformed LC atlas, voxels in the dilated LC region of interest with intensities greater than $I > \mu_{\text{ref}} + (4 * \sigma_{\text{ref}})$ were considered part of LC.

Table S1 shows the labels and MNI coordinates for all networks and ROIs discussed and were used to center a 5mm³ isotopic marker, including the LC (whose dilated voxels were split into rostral and caudal regions) (Deshpande et al., 2011, 2009; Stilla et al., 2007). BOLD signal from each voxel within an ROI were extracted and averaged to represent the overall signal for an ROI. This was repeated for 31 total ROIs: 9 from DMN, 7 from FPCN, 6 from DAN, 7 from SN, and 2 from LC. Although the LC is only a single ROI split into rostral and caudal portions, it is an entity distinguishable from the large-scale networks and will henceforth be referred to as a network in this paper.

3.1.1.5 Neuromelanin data acquisition and preprocessing

Neuromelanin MRI (NM-MRI) data were used to compute LC magnetization transfer contrast (MTC), which quantifies LC neuronal density and therefore quantifies the amount of neuromelanin in a subject's LC (Langley et al., 2020, 2017). Data were acquired using a magnetization-prepared 2D gradient recalled echo (GRE) sequence: TE/TR = 3.10/354 ms, 416 × 512 imaging matrix, 162 × 200 mm² (0.39 × 0.39 × 3 mm³) field of view, 15 slices, flip angle = 40°, four measurements, MTC preparation pulse (300°, 1.2 kHz off-resonance, 10 ms duration), and 470 Hz/pixel receiver bandwidth with a scan time of 10 minutes and 12 seconds (Chen et al., 2014; Langley et al., 2015). The four measurements were saved individually for offline registration and averaging. NM-MRI slices were prescribed perpendicular to the dorsal edge of the brainstem in the T₁-weighted image. Two subjects chose not to participate in the neuromelanin scans, so all NM-MRI data analyzed in this project were done with n = 28.

To process the NM-MRI data in FSL, images from the four GRE measurements were registered to the first image using a linear transformation tool in FLIRT and averaged (Smith et al., 2004; Woolrich et al., 2009). A transformation between this averaged NM-MRI image and T₁-weighted image was derived using a rigid body transform with boundary-based registration cost function in FLIRT. Prior to the rigid body transformation, the T₁-weighted image was parceled into gray matter, white matter, and cerebral spinal fluid regions. The quality of each registration between

T₁-weighted and NM-MRI images was assessed by overlaying the white matter-gray matter boundary from the T₁-weighted image on the NM-MRI image. No significant deviation was observed in all subjects. Contrast from the magnetization transfer preparation pulse, denoted MTC, was then calculated via

$$MTC = \frac{(I - I_{ref})}{I_{ref}} \quad (1)$$

where I denotes the intensity of a voxel in the NM-MRI image and I_{ref} refers to the mean intensity of a reference region in the NM-MRI image. To ensure consistent placement of reference region in NM-MRI images across subjects, a reference region was drawn in the pons in MNI T₁-weighted common space and then transformed to individual NM-MRI images. A LC atlas in MNI space was used in this study to localize the region around LC for MTC measurement (Langley et al., 2020). The LC atlas was transformed to NM-MRI space using the aforementioned transformations and using a threshold level of 0.5. After binarizing, each subject's mean MTC was measured in the LC ROI resulting in a total of $n = 28$ values. (Two subjects did not undergo the neuromelanin scans.)

3.2 Hidden Markov model

To identify hidden brain state patterns and dynamics, and how they changed as a function of LC activity, we fitted a Gaussian hidden Markov model (HMM) to the functional neuroimaging dataset following previously-published methods (Chen et al., 2016; Hussain et al., 2022; Stevner et al., 2019; Vidaurre et al., 2017). BOLD signals from the various ROIs (**Section 3.1.1.4; Supplementary Material Section S1**) were extracted, preprocessed, z-scored, and concatenated across subjects. Note that the data for RS0 and PostAr (SQ1-RS5) were z-scored separately within each condition because they formed four separate runs during acquisition, for a total of four z-scoring performed per subject: RS0 for active and sham, and SQ1-RS5 (PostAr) for active and sham. These fMRI time series were then concatenated timewise across all subjects to create a matrix of size (time * # subjects) x (# ROIs) and submitted as input to the `hmmlearn` package to be fit with standard procedures described elsewhere (Pedregosa et al., 2011). That is, the forward and Viterbi algorithms were used in conjunction to identify the most likely sequence of hidden states given the observable BOLD signal. The Baum-Welch algorithm was then implemented to calculate the transition and emission probabilities of a given state (Jurafsky and Martin, 2009; Rabiner and Juang, 1986; Rabiner, 1989).

To determine the optimal number of states for the HMM employed here, we employed two separate methods. These methods determined that a 5-state model fit the data best, and so all subsequent analyses and results presented here are for a 5-state HMM. See **Supplemental Material Section S2** for details.

3.3 Analysis of model outputs

We analyzed the outputs of the fitted HMM in a number of ways. First, we examined the state patterns themselves, i.e. how activity in each ROI changed as a function of state and across active versus sham control conditions. We also analyzed aspects of the trajectory through state space, including the Viterbi path itself, the percent of time spent in each state, the average state duration, and the transition probability matrices describing the model's behavior. These latter

measures describing state trajectories were calculated separately for RS0 and the “post-arousal” (PostAr) block containing SQ1-RS5, because this latter portion of the scan occurred after the handgrip task (both active and sham). They were then compared across active versus sham conditions as well as compared to baseline dynamics during RS0. Below, we describe each of these approaches in detail.

3.3.1 Exploring descriptive model outputs

3.3.1.1 Activation state pattern characterization

The HMM fitting procedure directly outputs mean state patterns, i.e. the average activity shown by each ROI for a given hidden state recovered by the model. We also analyzed activation state patterns specific to the active and sham conditions as a means of determining whether a certain state pattern was dominant in one condition and therefore driving the overall spatial patterns. In accordance with Chen and colleagues’ (Chen et al., 2016) method of state pattern acquisition, these spatial patterns were acquired by averaging the BOLD signal from TRs where the Viterbi path labeled a state to be active, for active and sham conditions separately. That is, for a given state within a given condition, we identified the TRs where that state was the most likely to be occupied by the subject, and then averaged across all those TRs to produce an average BOLD signal in each ROI that can be tied to each state within that condition. We refer to this process as the *Viterbi averaging method*.

We compared the states recovered via the *Viterbi averaging method* across active versus sham conditions by first calculating the Pearson correlation coefficient between active and sham for each state, where state was defined as the average state found across all subjects.

Second, we again calculated the Pearson correlation coefficient between active and sham for each state, but this time within each subject so that we could perform statistical analyses. After Fisher-z transforming the correlation coefficients such that the distribution of data would not violate the normality assumptions of an ANOVA, we conducted a one-way repeated measures ANOVA on the transformed coefficients to seek a main effect of state. A significant main effect was followed by t-tests against 0 within each state.

Finally, we also calculated on an individual subjects basis the Euclidean distance between active and sham conditions for each state and each subject. The purpose of this analysis was to determine whether LC MTC correlates with how different the states are across this condition manipulation, so that these distances were then Spearman correlated with LC MTC across subjects.

3.3.1.2 Viterbi path

The Viterbi path – a direct HMM output – was used to qualitatively assess differences between active and sham conditions and to obtain qualitative insight into the temporal dynamics of the LC dataset. Since the active and sham conditions were fitted together, the model provided the hidden state sequence for concatenated active and sham conditions. We therefore separated the first and second halves of the outputted Viterbi path to examine the active and sham state sequences separately.

3.3.2 Characterizing brain state behavior & covariance with LC structure

We next examined and characterized not only the states themselves, but how they behaved as a function of active versus sham conditions, and how these measures covaried with LC MTC across subjects. This allowed us to ask questions about how the squeezing task induced or changed transition into or occupancy of arousal-related states, including how LC neuronal density (quantified by LC MTC) was related to these brain state behaviors.

We note again that each of the measures described in this section was computed separately for RS0 versus PostAr (SQ1-RS5; see **Methods**). This is because RS0 provides a baseline before any prompts are shown to either squeeze (active condition) or raise the hand to the chest (sham control condition), and so provide a benchmark against which we can look for *changes* in each measure, corrected for individual differences across subjects and conditions (and before application of the covariate of LC MTC). This approach also provides a standardization across active and sham conditions, such that the critical questions centered on whether each metric's deviation from baseline is dependent on whether the subject was actively squeezing or not.

For all metrics described in this section, the first omnibus test typically took the form of computing the relevant metric separately in the active and sham conditions and in the RS0 and PostAr blocks, such that every subject had four measures of the metric in question. To do baseline correction within each scanning session (which occurred on two separate days; see **Methods Section 3.1.1.2**) we then subtract the RS0 metric from the PostAr metric, separately in the active and sham conditions. The resulting difference score is submitted to statistical tests as appropriate, detailed in the following sections.

Finally, to determine the degree to which LC structure mediated the relationships found via the analyses described below, we calculated the Spearman correlation between LC MTC and these measures; Spearman correlations were chosen because we had no *a priori* reason to believe LC MTC should be linearly related to any of these measures.

Below we describe these analyses in more detail.

3.3.2.1 Average state duration

After the hidden states were extracted and characterized, we were interested to know whether the propensity to dwell in each state, once reached, changes across conditions or states. Thus, we defined average state duration as the mean time spent in a state once a subject entered that state. This was computed for each subject by calculating the number of consecutive TRs spent in a state once the subjects entered it, and then averaging this number across the total number of times the subject entered that state, separately for the active and sham conditions and also separately within RS0 and PostAr blocks. This leaves us with four average state duration measures for each subject: $Dur_{RS0,active}$, $Dur_{RS0,sham}$, $Dur_{PostAr,active}$, and $Dur_{PostAr,sham}$. Finally, we subtracted RS0 from PostAr within each of the active and sham conditions to get a difference score, i.e.

$$\Delta Dur_i = Dur_{PostAr,i} - Dur_{RS0,i} \quad (2)$$

with i referring to condition, either active or sham. The resulting difference scores ΔDur were submitted to a 2 (condition: active vs sham) x 5 (state) repeated measures ANOVA. We then

conducted step-down ANOVAs and t-tests as appropriate; Greenhouse-Geisser corrections for sphericity violations were used as needed.

Finally, to examine the degree to which changes in average state duration as a function of condition were moderated by LC neuromelanin levels across subjects, we computed the Spearman correlation between LC MTC and average state duration within subsets of the data (condition and state) as appropriate.

3.3.2.2 Transition probabilities

A second question concerns how transition behavior changes as a function of active versus sham condition, and the degree to which these changes are moderated by LC MTC. A *transition probability matrix* (TPM) provides a summary of all the dynamics observed in the Viterbi path, in that the value contained in TPM_{ij} describes the probability of switching from state i to state j at any given moment in time. The TPM directly outputted from the HMM fitting procedure provides a general overview of transitions for both conditions as a whole, and also includes baseline (RS0) effects since it reflects the fitting procedure applied to all data concatenated across subjects and conditions. However, we were interested in changes in transition probabilities across the several manipulations of our task.

First, we were interested to see how the TPM changed from baseline once the handgrip task was introduced, i.e., during PostAr for both active and sham conditions. To calculate this, we concatenated Viterbi paths within each of the active and sham conditions, respectively, during the PostAr block and identified the number of times a subject transitioned out of a certain state and into another, then divided that value by the total number of transitions in the block (374). To remove the effects of baseline, the TPM was calculated similarly for RS0 separately in each condition, and then subtracted from the overall PostAr transition probability matrix (again separately in each condition) to produce a *relative transition probability matrix* (RTPM) for each condition $c \in \{Active, Sham\}$:

$$RTPM_c = TPM_{c,PostAr} - TPM_{c,RS0} \quad (3)$$

which describes the transition probabilities in the PostAr block relative to whatever baseline was set during RS0 for that subject during that scanning session.

Next, we checked for differences between $RTPM_{Active}$ and $RTPM_{Sham}$. To do this, we first computed the Euclidean distance between $RTPM_{Active}$ and $RTPM_{Sham}$ for each subject via

$$d_s(active, sham) = \sqrt{\sum_{i=1}^{20} (p_{active,i} - p_{sham,i})^2} \quad (4)$$

where d_s is the Euclidean distance between the transition probabilities for a particular transition $i \in \{S1 \rightarrow S2, S1 \rightarrow S3, \dots, S5 \rightarrow S4\}$ excluding self-transitions (i.e., 20 pairwise transitions in total), p is the transition probability for that particular state transition, and $s \in \{subjects\}$. d_s thus indexes the total distance between the active and sham RTPMs for a particular subject s , across all pairwise transitions. We compared the distribution of these distances to 0 using a nonparametric Wilcoxon sign rank test; this process is akin to a nonparametric paired t-test.

We were also interested in which particular pairwise transitions might drive these differences, so we next computed $p_{active,i} - p_{sham,j}$ for all pairwise transitions $i \rightarrow j$ within $RTPM_{Active}$ and $RTPM_{Sham}$ and for each subject, and tested whether each of these distributions was different from 0 across subjects with a series of Wilcoxon sign rank tests.

Finally, to determine whether LC neuromelanin content mediated changes in pairwise transition behavior – that is, differences between $RTPM_{Active}$ and $RTPM_{Sham}$ – we Spearman correlated the differences between $RTPM_{Active}$ and $RTPM_{Sham}$ with LC MTC across subjects.

3.3.2.3 Fractional occupancy

Finally, we were also interested in the percent of overall time that subjects spent in each hidden state. Was one state dominant over another, and did this change as a function of active versus sham condition and/or was it correlated with LC MTC? This is especially important because any differences in transition probabilities or state duration must be interpreted with respect to how much time, overall, a subject spent in each state: If a particular state becomes highly dominant in one condition over another, that might also carry increases in duration or transition probabilities into that particular state.

Therefore, we defined *fractional occupancy* (FO) as the proportion of time spent visiting a state. Fractional occupancy was calculated by first counting the total number of TRs each subject spent in a certain state for each block, RS0 and PostAr; that value was then divided by the total number of TRs in each block (150 for RS0 and 375 for PostAr) to obtain the fractional occupancy of each state separately within either RS0 or PostAr. We performed this calculation separately in the active versus sham conditions, and then subtracted RS0 from PostAr as done previously for average state duration. That is, we computed

$$\Delta FO_i = FO_{PostAr,i} - FO_{RS0,i} \quad (5)$$

with i again referring to condition, either active or sham. Following the previous design for average state duration, the resulting difference scores ΔFO were submitted to a 2 (condition: active vs sham) x 5 (state) repeated measures ANOVA. We then conducted step-down ANOVAs and t-tests as appropriate; Greenhouse-Geisser corrections for sphericity violations were used as needed, and any outliers more than 3 standard deviations from the mean in any condition were discarded. Finally, to examine the degree to which changes in fractional occupancy as a function of condition were moderated by LC neuromelanin, we again computed the Spearman correlation between LC MTC and fractional occupancy within subsets of the data (condition and state) as appropriate.

Data/code availability statement

Hidden Markov models were generated using the hmmlearn library in python (<https://github.com/hmmlearn/hmmlearn>). The fMRI dataset is available from the authors upon reasonable request.

Authorship contribution

Sana Hussain: Conceptualization, Formal Analysis, Investigation, Methodology, Project Administration, Software, Validation, Visualization, Writing -- Original Draft, Writing -- Review & Editing. **Isaac Menchaca**: Investigation, Methodology, Formal Analysis. **Mahsa Alizadeh Shalchy**: Investigation, Methodology. **Kimia Yaghoubi**: Investigation, Methodology. **Jason Langley**: Investigation, Methodology, Supervision, Validation, Visualization, Writing -- Review & Editing. **Aaron R. Seitz**: Conceptualization, Funding Acquisition, Investigation, Methodology, Project Administration, Supervision, Validation, Visualization, Writing -- Review & Editing. **Xiaoping P. Hu**: Conceptualization, Funding Acquisition, Investigation, Methodology, Project Administration, Resources, Supervision, Validation, Visualization, Writing -- Review & Editing. **Megan A. K. Peters**: Conceptualization, Funding Acquisition, Investigation, Methodology, Project Administration, Resources, Supervision, Validation, Visualization, Writing -- Original Draft, Writing -- Review & Editing.

Declaration of competing interests

None

Acknowledgements

This work was supported in part by the UCR NASA MIRO FIELDS Fellowship (to Sana Hussain). Data collection and sharing for this project was provided by the Human Connectome Project (HCP; Principal Investigators: Bruce Rosen, M.D., Ph.D., Arthur W. Toga, Ph.D., Van J. Weeden, MD). HCP funding was provided by the National Institute of Dental and Craniofacial Research (NIDCR), the National Institute of Mental Health (NIMH), and the National Institute of Neurological Disorders and Stroke (NINDS). HCP data are disseminated by the Laboratory of Neuro Imaging at the University of Southern California. This work was funded by NIA R01 NS108638-01 (PIs: Xiaoping P. Hu and Aaron R. Seitz) and by the Canadian Institute for Advanced Research Azrieli Global Scholars Program (PI: Megan A. K. Peters). Funding sources had no involvement in the design and methodology of the study.

References

- Aston-Jones G, Cohen JD. 2005. An integrative theory of locus coeruleus-norepinephrine function: adaptive gain and optimal performance. *Annu Rev Neurosci* **28**:403–450.
- Baker AP, Brookes MJ, Rezek IA, Smith SM, Behrens T, Probert Smith PJ, Woolrich M. 2014. Fast transient networks in spontaneous human brain activity. *Elife* **3**:e01867.
- Braak H, Del Tredici K, Rüb U, de Vos RAI, Jansen Steur ENH, Braak E. 2003. Staging of brain pathology related to sporadic Parkinson's disease. *Neurobiol Aging* **24**:197–211.
- Braak H, Thal DR, Ghebremedhin E, Del Tredici K. 2011. Stages of the pathologic process in Alzheimer disease: age categories from 1 to 100 years. *J Neuropathol Exp Neurol* **70**:960–969.
- Brett M, Johnsrude IS, Owen AM. 2002. The problem of functional localization in the human brain. *Nat Rev Neurosci* **3**:243–249.
- Chen S, Langley J, Chen X, Hu X. 2016. Spatiotemporal Modeling of Brain Dynamics Using Resting-State Functional Magnetic Resonance Imaging with Gaussian Hidden Markov Model. *Brain Connect* **6**:326–334.
- Chen X, Huddleston DE, Langley J, Ahn S, Barnum CJ, Factor SA, Levey AI, Hu X. 2014. Simultaneous imaging of locus coeruleus and substantia nigra with a quantitative neuromelanin MRI approach. *Magn Reson Imaging* **32**:1301–1306.
- Clewett DV, Lee T-H, Greening S, Ponzio A, Margalit E, Mather M. 2016. Neuromelanin marks the spot: identifying a locus coeruleus biomarker of cognitive reserve in healthy aging. *Neurobiol Aging* **37**:117–126.
- Deshpande G, LaConte S, James GA, Peltier S, Hu X. 2009. Multivariate Granger causality analysis of fMRI data. *Hum Brain Mapp* **30**:1361–1373.
- Deshpande G, Santhanam P, Hu X. 2011. Instantaneous and causal connectivity in resting state brain networks derived from functional MRI data. *Neuroimage* **54**:1043–1052.
- Dixon ML, De La Vega A, Mills C, Andrews-Hanna J, Spreng RN, Cole MW, Christoff K. 2018. Heterogeneity within the frontoparietal control network and its relationship to the default and dorsal attention networks. *Proc Natl Acad Sci U S A* **115**:E1598–E1607.
- Eavani H, Satterthwaite TD, Gur RE, Gur RC, Davatzikos C. 2013. Unsupervised Learning of Functional Network Dynamics in Resting State fMRI. *Information Processing in Medical Imaging*. Springer Berlin Heidelberg. pp. 426–437.
- Eddy SR. 2004. What is a hidden Markov model? *Nat Biotechnol* **22**:1315–1316.
- Glover GH, Li TQ, Ress D. 2000. Image-based method for retrospective correction of physiological motion effects in fMRI: RETROICOR. *Magn Reson Med* **44**:162–167.
- Greicius MD, Menon V. 2004. Default-Mode Activity during a Passive Sensory Task: Uncoupled from Deactivation but Impacting Activation. *Journal of Cognitive Neuroscience*. doi:10.1162/0898929042568532
- Guedj C, Meunier D, Meunier M, Hadj-Bouziane F. 2017. Could LC-NE-Dependent Adjustment of Neural Gain Drive Functional Brain Network Reorganization? *Neural Plast* **2017**:4328015.
- Hussain S, Langley J, Seitz AR, Peters MAK, Hu XP. 2022. A novel hidden Markov approach to studying dynamic functional connectivity states in human neuroimaging. *bioRxiv*. doi:10.1101/2022.02.02.478844
- Hussain S, Shalchy MA, Yaghoubi KC, Langley J, Chen X, Bennett I, Huang R, Clewett D, Nelson SE, Velasco R, Kennedy B, Han S, Tu K, Seitz AR, Zhang N, Mather M, Hu X, Peters MAK. 2019. Locus Coeruleus Engagement Drives Network Connectivity Dynamics In Humans And Rats. *Cognitive Computational Neuroscience* 2019.
- Joshi S, Li Y, Kalwani RM, Gold JI. 2016. Relationships between Pupil Diameter and Neuronal Activity in the Locus Coeruleus, Colliculi, and Cingulate Cortex. *Neuron* **89**:221–234.

- Jurafsky D, Martin JH. 2009. Speech and Language Processing: An Introduction to Natural Language Processing, Computational Linguistics, and Speech Recognition. Prentice Hall.
- Keren NI, Lozar CT, Harris KC, Morgan PS, Eckert MA. 2009. In vivo mapping of the human locus coeruleus. *Neuroimage* **47**:1261–1267.
- Khiatani D, Ghose U. 2017. Weather forecasting using Hidden Markov Model 2017 International Conference on Computing and Communication Technologies for Smart Nation (IC3TSN). pp. 220–225.
- Kozłowski S, Brzezinska Z, Nazar K, Kowalski W, Franczyk M. 1973. Plasma catecholamines during sustained isometric exercise. *Clin Sci Mol Med* **45**:723–731.
- Kundu P, Inati SJ, Evans JW, Luh W-M, Bandettini PA. 2012. Differentiating BOLD and non-BOLD signals in fMRI time series using multi-echo EPI. *Neuroimage* **60**:1759–1770.
- Laird AR, Lancaster JL, Fox PT. 2005. BrainMap: the social evolution of a human brain mapping database. *Neuroinformatics* **3**:65–78.
- Lake CR, Ziegler MG, Kopin IJ. 1976. Use of plasma norepinephrine for evaluation of sympathetic neuronal function in man. *Life Sci* **18**:1315–1325.
- Lancaster JL, Tordesillas-Gutiérrez D, Martínez M, Salinas F, Evans A, Zilles K, Mazziotta JC, Fox PT. 2007. Bias between MNI and Talairach coordinates analyzed using the ICBM-152 brain template. *Hum Brain Mapp* **28**:1194–1205.
- Langley J, Huddleston DE, Chen X, Sedlacik J, Zachariah N, Hu X. 2015. A multicontrast approach for comprehensive imaging of substantia nigra. *NeuroImage*. doi:10.1016/j.neuroimage.2015.02.045
- Langley J, Huddleston DE, Liu CJ, Hu X. 2017. Reproducibility of locus coeruleus and substantia nigra imaging with neuromelanin sensitive MRI. *MAGMA* **30**:121–125.
- Langley J, Hussain S, Flores JJ, Bennett IJ, Hu X. 2020. Characterization of age-related microstructural changes in locus coeruleus and substantia nigra pars compacta. *Neurobiol Aging* **87**:89–97.
- Langley J, Hussain S, Huddleston DE, Bennett IJ, Hu XP. 2021. Impact of Locus Coeruleus and Its Projections on Memory and Aging. *Brain Connect*. doi:10.1089/brain.2020.0947
- Lindquist MA, Waugh C, Wager TD. 2007. Modeling state-related fMRI activity using change-point theory. *NeuroImage*. doi:10.1016/j.neuroimage.2007.01.004
- Liu KY, Marijatta F, Hämmerer D, Acosta-Cabronero J, Düzel E, Howard RJ. 2017. Magnetic resonance imaging of the human locus coeruleus: A systematic review. *Neurosci Biobehav Rev* **83**:325–355.
- Liu W, Awate SP, Anderson JS, Thomas Fletcher P. 2014. A functional network estimation method of resting-state fMRI using a hierarchical Markov random field. *NeuroImage*. doi:10.1016/j.neuroimage.2014.06.001
- Manaye KF, McIntire DD, Mann DM, German DC. 1995. Locus coeruleus cell loss in the aging human brain: a non-random process. *J Comp Neurol* **358**:79–87.
- Marmon AR, Enoka RM. 2010. Comparison of the influence of two stressors on steadiness during index finger abduction. *Physiol Behav* **99**:515–520.
- Ma SY, Röytt M, Collan Y, Rinne JO. 1999. Unbiased morphometrical measurements show loss of pigmented nigral neurones with ageing. *Neuropathol Appl Neurobiol* **25**:394–399.
- Mather M, Clewett D, Sakaki M, Harley CW. 2016. GANEing traction: The broad applicability of NE hotspots to diverse cognitive and arousal phenomena. *Behav Brain Sci* **39**:e228.
- Mather M, Harley CW. 2016. The Locus Coeruleus: Essential for Maintaining Cognitive Function and the Aging Brain. *Trends Cogn Sci* **20**:214–226.
- Mather M, Huang R, Clewett D, Nielsen SE, Velasco R, Tu K, Han S, Kennedy BL. 2020. Isometric exercise facilitates attention to salient events in women via the noradrenergic system. *Neuroimage* **210**:116560.
- Mather M, Yoo HJ, Clewett DV, Lee T-H, Greening SG, Ponzio A, Min J, Thayer JF. 2017. Higher locus coeruleus MRI contrast is associated with lower parasympathetic influence

- over heart rate variability. *NeuroImage*. doi:10.1016/j.neuroimage.2017.02.025
- Megemont M, McBurney-Lin J, Yang H. 2022. Pupil diameter is not an accurate real-time readout of locus coeruleus activity. *Elife* **11**. doi:10.7554/eLife.70510
- Menon V, Uddin LQ. 2010. Saliency, switching, attention and control: a network model of insula function. *Brain Structure and Function*. doi:10.1007/s00429-010-0262-0
- Murphy PR, O'Connell RG, O'Sullivan M, Robertson IH, Balsters JH. 2014. Pupil diameter covaries with BOLD activity in human locus coeruleus. *Hum Brain Mapp* **35**:4140–4154.
- Nielsen SE, Barber SJ, Chai A, Clewett DV, Mather M. 2015. Sympathetic arousal increases a negative memory bias in young women with low sex hormone levels. *Psychoneuroendocrinology* **62**:96–106.
- Nielsen SE, Mather M. 2015. Comparison of two isometric handgrip protocols on sympathetic arousal in women. *Physiol Behav* **142**:5–13.
- O'Reilly JX, Woolrich MW, Behrens TEJ, Smith SM, Johansen-Berg H. 2012. Tools of the trade: psychophysiological interactions and functional connectivity. *Soc Cogn Affect Neurosci* **7**:604–609.
- Ou J, Xie L, Jin C, Li X, Zhu D, Jiang R, Chen Y, Zhang J, Li L, Liu T. 2015. Characterizing and Differentiating Brain State Dynamics via Hidden Markov Models. *Brain Topogr* **28**:666–679.
- Oyarzún JP, Lopez-Barroso D, Fuentemilla L, Cucurell D, Pedraza C, Rodriguez-Fornells A, de Diego-Balaguer R. 2012. Updating fearful memories with extinction training during reconsolidation: a human study using auditory aversive stimuli. *PLoS One* **7**:e38849.
- Pedregosa F, Varoquaux G, Gramfort A, Michel V, Thirion B, Grisel O, Blondel M, Prettenhofer P, Weiss R, Dubourg V, Vanderplas J, Passos A, Cournapeau D, Brucher M, Perrot M, Duchesnay É. 2011. Scikit-learn: Machine Learning in Python. *J Mach Learn Res* **12**:2825–2830.
- Quian Quiroga R, Garcia H. 2003. Single-trial event-related potentials with wavelet denoising. *Clin Neurophysiol* **114**:376–390.
- Rabiner L, Juang B. 1986. An introduction to hidden Markov models. *IEEE ASSP Magazine*. doi:10.1109/massp.1986.1165342
- Rabiner LR. 1989. A tutorial on hidden Markov models and selected applications in speech recognition. *Proceedings of the IEEE*. doi:10.1109/5.18626
- Raichle ME. 2015. The brain's default mode network. *Annu Rev Neurosci* **38**:433–447.
- Raichle ME. 2011. The restless brain. *Brain Connect* **1**:3–12.
- Redondo J, Fraga I, Padrón I, Piñeiro A. 2008. Affective ratings of sound stimuli. *Behav Res Methods* **40**:784–790.
- Robinson LF, Wager TD, Lindquist MA. 2010. Change point estimation in multi-subject fMRI studies. *Neuroimage* **49**:1581–1592.
- Sara SJ. 2016. Locus coeruleus reports changes in environmental contingencies. *Behav Brain Sci* **39**:e223.
- Sara SJ. 2015. Locus Coeruleus in time with the making of memories. *Curr Opin Neurobiol* **35**:87–94.
- Sara SJ. 2009. The locus coeruleus and noradrenergic modulation of cognition. *Nat Rev Neurosci* **10**:211–223.
- Schwabe L, Schächinger H. 2018. Ten years of research with the Socially Evaluated Cold Pressor Test: Data from the past and guidelines for the future. *Psychoneuroendocrinology* **92**:155–161.
- Shappell H, Caffo BS, Pekar JJ, Lindquist MA. 2019. Improved state change estimation in dynamic functional connectivity using hidden semi-Markov models. *Neuroimage* **191**:243–257.
- Shibata E, Sasaki M, Tohyama K, Kanbara Y, Otsuka K, Ehara S, Sakai A. 2006. Age-related changes in locus ceruleus on neuromelanin magnetic resonance imaging at 3 Tesla. *Magn Reson Med Sci* **5**:197–200.

- Smith SM, Jenkinson M, Woolrich MW, Beckmann CF, Behrens TEJ, Johansen-Berg H, Bannister PR, De Luca M, Drobnjak I, Flitney DE, Niazy RK, Saunders J, Vickers J, Zhang Y, De Stefano N, Brady JM, Matthews PM. 2004. Advances in functional and structural MR image analysis and implementation as FSL. *Neuroimage* **23 Suppl 1**:S208–19.
- Song AH, Kucyi A, Napadow V, Brown EN, Loggia ML, Akeju O. 2017. Pharmacological Modulation of Noradrenergic Arousal Circuitry Disrupts Functional Connectivity of the Locus Coeruleus in Humans. *J Neurosci* **37**:6938–6945.
- Stark R, Wolf OT, Tabbert K, Kagerer S, Zimmermann M, Kirsch P, Schienle A, Vaitl D. 2006. Influence of the stress hormone cortisol on fear conditioning in humans: evidence for sex differences in the response of the prefrontal cortex. *Neuroimage* **32**:1290–1298.
- Stevner ABA, Vidaurre D, Cabral J, Rapuano K, Nielsen SFV, Tagliazucchi E, Laufs H, Vuust P, Deco G, Woolrich MW, Van Someren E, Kringelbach ML. 2019. Discovery of key whole-brain transitions and dynamics during human wakefulness and non-REM sleep. *Nat Commun* **10**:1035.
- Stilla R, Deshpande G, LaConte S, Hu X, Sathian K. 2007. Posteromedial parietal cortical activity and inputs predict tactile spatial acuity. *J Neurosci* **27**:11091–11102.
- Vecht RJ, Graham GW, Sever PS. 1978. Plasma noradrenaline concentrations during isometric exercise. *Br Heart J* **40**:1216–1220.
- Vidaurre D, Abeysuriya R, Becker R, Quinn AJ, Alfaro-Almagro F, Smith SM, Woolrich MW. 2018a. Discovering dynamic brain networks from big data in rest and task. *Neuroimage* **180**:646–656.
- Vidaurre D, Hunt LT, Quinn AJ, Hunt BAE, Brookes MJ, Nobre AC, Woolrich MW. 2018b. Spontaneous cortical activity transiently organises into frequency specific phase-coupling networks. *Nat Commun* **9**:2987.
- Vidaurre D, Quinn AJ, Baker AP, Dupret D, Tejero-Cantero A, Woolrich MW. 2016. Spectrally resolved fast transient brain states in electrophysiological data. *Neuroimage* **126**:81–95.
- Vidaurre D, Smith SM, Woolrich MW. 2017. Brain network dynamics are hierarchically organized in time. *Proc Natl Acad Sci U S A* **114**:12827–12832.
- Wallin BG, Esler M, Dorward P, Eisenhofer G, Ferrier C, Westerman R, Jennings G. 1992. Simultaneous measurements of cardiac noradrenaline spillover and sympathetic outflow to skeletal muscle in humans. *J Physiol* **453**:45–58.
- Wallin BG, Mörlin C, Hjemdahl P. 1987. Muscle sympathetic activity and venous plasma noradrenaline concentrations during static exercise in normotensive and hypertensive subjects. *Acta Physiol Scand* **129**:489–497.
- Woolrich MW, Jbabdi S, Patenaude B, Chappell M, Makni S, Behrens T, Beckmann C, Jenkinson M, Smith SM. 2009. Bayesian analysis of neuroimaging data in FSL. *NeuroImage*. doi:10.1016/j.neuroimage.2008.10.055
- Yaghoubi KC, Shalchy MA, Hussain S, Chen X, Bennett IJ, Mather M, Hu X, Seitz AR, Peters MAK. 2019. Computational fMRI Reveals Separable Representations Of Stimulus and Choice In Auditory Cortex: A Tool for Studying the Locus Coeruleus Circuit. *Cognitive Computational Neuroscience* 2019.
- Yang H, Bari BA, Cohen JY, O'Connor DH. 2021. Locus coeruleus spiking differently correlates with S1 cortex activity and pupil diameter in a tactile detection task. *Elife* **10**. doi:10.7554/eLife.64327
- Yang Z, LaConte S, Weng X, Hu X. 2008. Ranking and averaging independent component analysis by reproducibility (RAICAR). *Hum Brain Mapp* **29**:711–725.
- Zecca L, Stroppolo A, Gatti A, Tampellini D, Toscani M, Gallorini M, Giaveri G, Arosio P, Santambrogio P, Fariello RG, Karatekin E, Kleinman MH, Turro N, Hornykiewicz O, Zucca FA. 2004. The role of iron and copper molecules in the neuronal vulnerability of locus coeruleus and substantia nigra during aging. *Proc Natl Acad Sci U S A* **101**:9843–9848.
- Zhang M, Jiang X, Fang Z, Zeng Y, Xu K. 2019. High-order Hidden Markov Model for trend

prediction in financial time series. *Physica A: Statistical Mechanics and its Applications* **517**:1–12.

Zucca FA, Bellei C, Giannelli S, Terreni MR, Gallorini M, Rizzio E, Pezzoli G, Albertini A, Zecca L. 2006. Neuromelanin and iron in human locus coeruleus and substantia nigra during aging: consequences for neuronal vulnerability. *J Neural Transm* **113**:757–767.

Supplementary material

S1. Regions of interest

ROI	Abbrv.	Full Name	MNI (x,y,z)	Source
Default Mode Network				
1	PCC	Posterior Cingulate Cortex	(2,54,16)	Deshpande et al. 2011
2	L pIPL	Left Posterior Inferior Parietal Lobule	(-46,-72,28)	Deshpande et al. 2011
3	R pIPL	Right Posterior Inferior Parietal Lobule	(50,-64,26)	Deshpande et al. 2011
4	OFC/vACC	Orbitofrontal Cortex/Ventral Anterior Cingulate Cortex	(4,30,26)	Deshpande et al. 2011
5	dMPFC BA 8	Dorsomedial Prefrontal Cortex Brodmann Area 8	(-14,54,34)	Deshpande et al. 2011
6	dMPFC BA 9	Dorsomedial Prefrontal Cortex Brodmann Area 9	(22,58,26)	Deshpande et al. 2011
7	L DLPFC	Left Dorsolateral Prefrontal Cortex	(-50,20,34)	Deshpande et al. 2011
8	L PHG	Left Parahippocampal Gyrus	(-10,-38,-2)	Deshpande et al. 2011
9	L ITC	Left Inferolateral Temporal Cortex	(-60,-20,-18)	Deshpande et al. 2011
Fronto-Parietal Control Network				
1	L aPFC	Left Anterior Prefrontal Cortex	(-36,56,10,)	Deshpande et al. 2011
2	R aPFC	Right Anterior Prefrontal Cortex	(34,52,10)	Deshpande et al. 2011
3	R DLPFC	Right Dorsolateral Prefrontal Cortex	(46,14,42)	Deshpande et al. 2011
4	L aINS	Left Anterior Insula	(-30,20,-2)	Deshpande et al. 2011
5	R aINS	Right Anterior Insula	(32,22,-2)	Deshpande et al. 2011
6	L aIPL	Left Anterior Inferior Parietal Lobule	(-52,-50,46)	Deshpande et al. 2011
7	R aIPL	Right Anterior Inferior Parietal Lobule	(52,-46,46)	Deshpande et al. 2011
Dorsal Attention Network				
1	L MT	Left MidThalamus	(-44,-64,-2)	Deshpande et al. 2011
2	R MT	Right MidThalamus	(50,-70,-4)	Deshpande et al. 2011
3	L FEF	Left Frontal Eye Field	(-24,-8,50)	Deshpande et al. 2011
4	R FEF	Right Frontal Eye Field	(28,-10,50)	Deshpande et al. 2011

5	L SPL	Left Superior Parietal Lobule	(-26,-52,56)	Deshpande et al. 2011
6	R SPL	Right Superior Parietal Lobule	(24,-56,-54)	Deshpande et al. 2011
Saliency Network				
1	DAC	Dorsal Anterior Cingulate	(0,-22,36)	Raichle 2011
2	L aPFC	Left Anterior PFC	(-34,44,30)	Raichle 2011
3	R aPFC	Right Anterior PFC	(32,44,30)	Raichle 2011
4	L Insula	Left Insula	(-40,2,6)	Raichle 2011
5	R Insula	Right Insula	(42,2,6)	Raichle 2011
6	L LP	Left Lateral Parietal	(-62,-46,30)	Raichle 2011
7	R LP	Right Lateral Parietal	(62,-46,30)	Raichle 2011
Locus Coeruleus				
1	R LC	Rostral locus coeruleus	left (-3.0, -36.7, -20.4) right (4.4, -36.4, -19.5) (Probabilistic atlas)	Langley et al. 2020
2	C LC	Caudal locus coeruleus	left (-5.9, -38.1, -29.9) right (7.0, -38.1, -30.3) (Probabilistic atlas)	Langley et al. 2020

Table S1. List of MNI coordinates used for ROIs in the default mode network (DMN), fronto-parietal control network (FPCN), dorsal attention network (DAN), salience network (SN), and locus coeruleus (LC). Talaraich coordinates for DMN, FPCN, and DAN were taken from Deshpande et al. (Deshpande et al., 2011) and were converted to MNI using (Brett et al., 2002; Deshpande et al., 2011; Laird et al., 2005; Lancaster et al., 2007) while MNI coordinates for SN were taken directly from Raichle 2011 (Raichle, 2011). MNI coordinates for LC were taken from (Langley et al., 2017).

S2. Determining number of hidden states (stability analyses)

HMMs are fitted with an *a priori* defined number of hidden states, so we must first find that number before we can fit the model. For succinctness, in this section and the accompanying results section below we refer to the number of hidden states of a particular HMM instantiation as the *model order*. To determine the optimal model order for the HMM used here, we employed two separate methods.

First, following previous approaches we adopted the Ranking and Averaging Independent Component Analysis by Reproducibility (RAICAR) method (Chen et al., 2016; Hussain et al., 2022; Yang et al., 2008); this approach computes the ‘stability’ of recovered hidden state patterns to determine the appropriateness of a given *a priori* specified model order. Here, we

examined the stability of model orders 3-15 through computing Pearson correlations among states recovered across three initializations of the HMM fitting procedure: one with uniform starting probability of residing in all states, and two with randomly assigned starting probabilities. Note that, because within a given initialization the labeling of each state as “state 1” or “state 2” is arbitrary, in order to assess whether the recovered states are actually the same across initializations, we must first ‘match’ them up. We accomplished this matching via Pearson correlations, such that e.g. state 1 from Initialization 2 was relabeled as state 2 just in case the Pearson correlation between that state and state 2 from Initialization 1 was higher than any other pairwise correlation. Thus, after relabeling, each state label across initializations universally corresponded to the same spatial pattern to the maximal extent possible. Within each state assignment, the matched state patterns were then Pearson correlated between all initializations to obtain $(\# \text{ states})! / 2! * (\# \text{ states} - 2)!$ Pearson’s R^2 values, thereby determining the maximal degree of similarity between the matched patterns for the model order being currently tested. Finally, these values were then averaged, sorted from largest to smallest, and plotted as a function of model order, and then compared to a critical threshold of $R = 0.9$. That is, for a given state to be considered ‘stable’ across those initializations of the model, we must be able to discover a pairing of (arbitrarily-labeled) states across those two initializations such that the correlation between the two states is 0.9 or higher. Previously, a stability threshold of 0.8 has been used when more ROIs are being tested (Chen et al., 2016; Yang et al., 2008), but here we examined only 31 ROIs and so opted for a more conservative threshold of 0.9. Model orders for which several states displayed ‘stability’ less than $R^2 = 0.9$ were considered unstable, i.e. too few or too many hidden states specified *a priori*. See the methods described previously by Hussain and colleagues (Hussain et al., 2022) for more detail.

As a second, confirmatory approach, we also employed Euclidean distances to assess model stability and model order. In this case, a smaller Euclidean distance between two matched states indicates a better correspondence between model initializations. We followed similar logic to that used in the RAICAR method, but with additional steps to ensure that states from Initialization 2 were optimally matched with states from Initialization 1 and then relabeled, and the same for Initialization 3. To do this, state assignments from two initializations, I_i and I_j , within a certain model order were permuted and their spatial patterns matched via the smallest Euclidean distance such that each state universally corresponded to the same spatial pattern. For example, after permuting the state assignments from I_i and I_j , the Euclidean distance between state 1 from I_i and all states from I_j are computed. The results may show that the smallest Euclidean distance was computed with state 5 from I_j indicating that state 1 from R_i best corresponds to state 5 from R_j . State 5 from I_j would thus be relabeled as state 1 from I_j , then the process is repeated between state 2 from R_i and all states from I_j (except the relabeled state 1 as it has already been matched). This permutation-and-matching procedure was performed 100 times for all pairs of realizations (where matching $I_i \rightarrow I_j$ is not distinguished from matching $I_j \rightarrow I_i$) to ensure that the spatial patterns are paired uniquely without any bias of state assignment. This was repeated for a range of model orders generating a total of $100 * \left(\frac{(\# \text{ states})!}{2!(\# \text{ states} - 2)!} \text{ realizations} \right) * (\# \text{ states})$ values for a particular model order which are then averaged to represent its overall stability. This single average was plotted as a function of model order producing a curve where the smallest value succeeded by continuously increasing values for higher model orders indicates the optimal number of states for a dataset. Although this may seem similar to the RAICAR-based method, the Euclidean distance based method is more conservative because stability is assessed by ensuring that the average of hundreds of Euclidean distances is below a prespecified threshold rather than the average of a handful of R^2 values.

Figure S1 shows the results from performing the RAICAR-based and Euclidean distance-based stability analyses for model orders 3-15 using three initializations. Both plots indicate that five states were best for this investigation. This was the maximum model order where the stability values for all states remained above the predetermined threshold, and where the Euclidean distance remained as low as possible (zero) before dramatically increasing. Chen et al. 2016 (Chen et al., 2016) and Yang et al. 2008 (Yang et al., 2008) both used the RAICAR-based method, explored 236 ROIs and 162 independent components respectively, and employed a stability threshold of 0.8 (Chen et al., 2016; Yang et al., 2008). As discussed above we used a 0.9 threshold because we examined substantially fewer ROIs (Sara, 2009) so our analyses and interpretations could afford to be more stringent. However, whether we used a threshold of 0.9 or 0.8 at least one stability value for model orders six and above fell below 0.8; so, a 5-state model was selected via both standards.

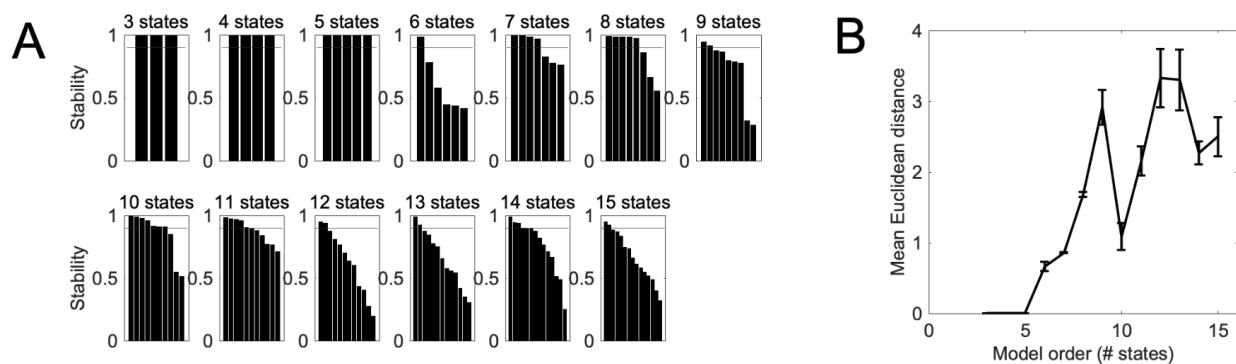


Figure S1. Results of stability analysis to determine HMM model order (number of hidden states). Stability analysis results via both the (A) RAICAR-based (B) and ED-based methods for model orders 3-15 indicate that a 5-state model was best, as this is the largest model order where the stability values were above the 0.9 threshold (thin horizontal lines) in the RAICAR-based results and the mean Euclidean distance was as small as possible with the largest number of states in the Euclidean distance-based results.

S3. Pupillometry

We also collected simultaneous pupillary dilation as a proxy for LC activity, as a confirmatory physiological measure. Fluctuations in pupil diameter have been validated in animal models using invasive recordings (Joshi et al., 2016; Keren et al., 2009), allowing them to be used as a noninvasive proxy measure for LC activity when simultaneously recorded with fMRI in humans (Joshi et al., 2016; Keren et al., 2009; Murphy et al., 2014). As noted below, however, technical challenges during data collection and relatively sparsity of data due to stringent exclusion requirements precluded strong conclusions being drawn via the pupillometry data and analyses. For completeness, here we present the exploratory analyses we were able to conduct, and show how they qualitatively align with the findings presented in the main text.

S3.1 Pupillometry methods

S3.1.1 Pupillometry data acquisition and preprocessing

Pupillometry data were collected using a TRACKPixx3 MRI/MEG (VPixx Technologies, Saint-Bruno, QC Canada), an MRI compatible binocular eye tracker, with sampling rate of 2kHz. Data were preprocessed using the ET-remove artifacts toolbox (<https://github.com/EmotionCognitionLab/ET-remove-artifacts>), time-shifted by three TRs to align with the hemodynamic response function delay (Murphy et al., 2014), and downsampled to match the temporal resolution of the fMRI data by averaging within each TR (Mather et al., 2020). The measure of interest is percent signal change so that we may measure pupil dilations relative to baseline; therefore, each subject's pupil dilation time series during PostAr blocks was divided by that subject's mean pupil dilation during RS0. Three subjects' data were unfortunately unusable due to technical difficulties during collection procedures, resulting in $n = 27$ for most pupillometry-related calculations. These three subjects were different from the ones who decided not to participate in the neuromelanin scans.

S3.1.2 Pupillometry analyses

Pupillometry analyses paralleled some of the state space trajectory analyses (see main text). Specifically, we computed the mean pupil dilation changes for state-specific pairwise transitions as a function of condition (active vs sham) to further explore how LC activity may be related to brain state behaviors. Pupil dilation changes as a function of state switching were computed by identifying a switch in subjects' state sequences, then calculating the difference between the normalized pupil size two TRs before the switch and the first TR after the switch. This calculation was contingent on the subject remaining in the same state for two TRs before or after the identified switch to ensure that they settled into a stable state. We cannot be less stringent with the criterion of remaining in the same state for two TRs before and after the switch because these criteria ensure that changes in pupil size were accompanying specific transitions, and that dilations/contractions from previous or succeeding transitions did not bleed into that calculation. After calculating these differences, the mean of these differences within a subject was found.

Once the mean subject-specific changes in pupil size during state specific transitions were found for both conditions (active and sham), the differences in these values were computed to reveal how pupil dilation changes at specific state transition points might vary due to active squeezing versus sham control. Finally, these differences were Spearman correlated with LC MTC to determine whether LC neuromelanin content impacted pupil dilation during switches between HMM-derived latent brain states. Because some subjects' data were missing due to improper data collection or the aforementioned exclusion criteria, only subjects whose data were accounted for in both the pupillometry and neuromelanin datasets were included in these correlations (at most $n = 25$).

S3.2 Pupillometry results and discussion

In the main text, we saw that the duration spent in S4 once it is entered was correlated with LC MTC (**Results Section 2.3.1**), as were changes in transition probabilities between the active and sham condition specifically regarding transitioning from S5→S4. We interpreted these results to mean that LC structure (neuromelanin and cell density) plays a meaningful role in the effectiveness of the squeeze manipulation and its consequent effects on brain dynamics, even in the cohort of healthy young adults used here. This is consistent with previous results showing similar causal relationships among LC structure integrity and arousal states in older adults (Hussain et al., 2019; Langley et al., 2021, 2020; Mather and Harley, 2016).

However, because of LC's small size (~2mm in diameter), it is difficult to establish whether LC activity itself (measured via the BOLD response) could also drive these behaviors, a problem that is exacerbated by the poor temporal resolution of fMRI. Therefore, as a confirmatory analysis, we turned next to pupillometry data as a proxy for LC activation. As introduced above, pupillary diameter has been established as a viable proxy for LC activity levels (Joshi et al., 2016; Keren et al., 2009; Murphy et al., 2014), which makes this measure valuable as a mitigation strategy for the noisiness of LC BOLD signal in fMRI due to the small size of LC.

Importantly, we highlight here that the goal of this analysis was to establish consistency with the results presented in the main text. Unfortunately, due to technical challenges and our stringent criteria for establishing pupil dilation changes as a function of state transition, pupil diameter data was unavailable for some subjects for some analyses (described in detail below). Therefore, we present these results as qualitative confirmation of the patterns identified in the main text, and future studies should seek to remedy the technical challenges we experienced so that a fuller understanding may be gained.

First, we calculated the mean changes in pupil dilation (**Supplementary Material Section S3.1**) for each pairwise transition between two states, separately as a function of active (**Figure S2A**) and sham (**Figure S2B**) conditions. We then found the difference between them (**Figure S2C**) to highlight distinct pupil size changes resulting from LC activity up-regulation. Finally, the difference in pupil dilation for state-specific transitions across conditions (prior to taking the global average across subjects) was correlated with LC MTC (**Figure S2D**). The criterion that subjects must remain in the same state for two TRs before and after the switch was enforced resulting in different numbers of subjects meeting this standard for a transition and consequent correlation with LC MTC (**Figure S2E**; see also **Supplementary Material Section S3.1**).

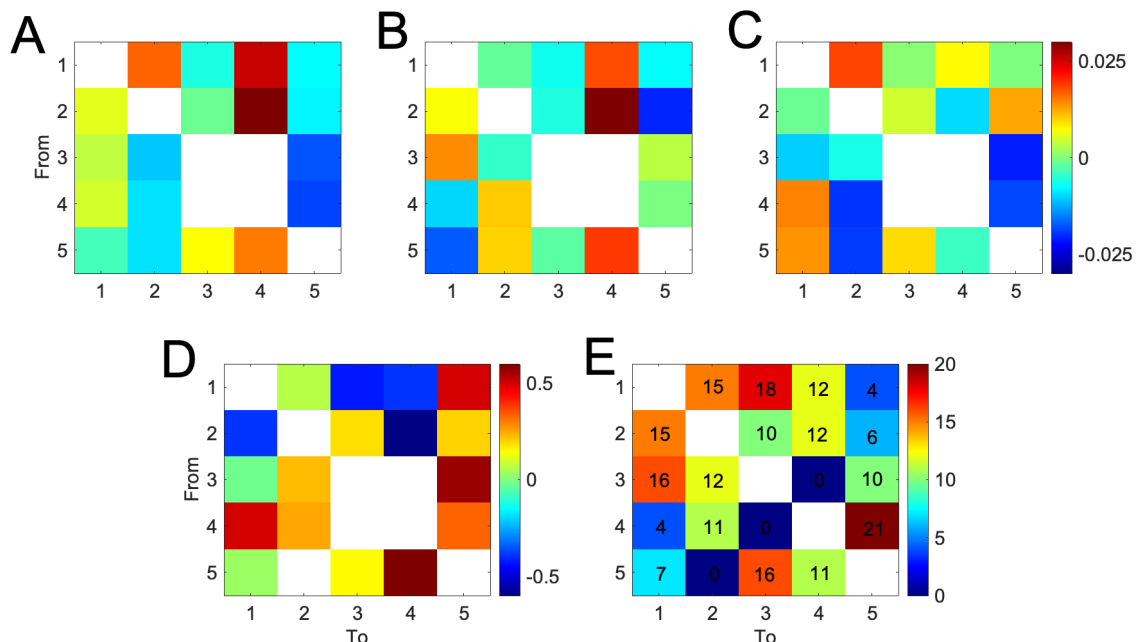


Figure S2. Pupil dilations changes for **(A)** active and **(B)** sham conditions as well as **(C)** the difference between them when subjects transitioned between specific states. **(D)** The difference in pupil dilation changes relative to baseline across conditions was correlated with LC MTC. We computed pupil dilation change for a transition only when

the subject remained in the same state for two TRs before and after an identified switch. Not all subjects underwent a switch that met this criterion, so **(E)** shows the number of subjects that experienced each transition. The largest changes in transition-specific pupil dilation to correlate with LC MTC **(D)** occurred for pairwise transitions $S1 \rightarrow S5$, $S3 \rightarrow S5$, $S4 \rightarrow S1$, and $S5 \rightarrow S4$. Interestingly, three of these four ($S1 \rightarrow S5$, $S4 \rightarrow S1$, and $S5 \rightarrow S4$) coincide precisely with the only three transitions that showed significant changes in relative transition probability matrices (RTPMs; **Figure 5**), and the largest of these ($S5 \rightarrow S4$) is precisely for the transition that previously showed significant correlation with LC MTC. That is, LC MTC predicted how pupil would react in these specific transitions, and these were also the specific transitions that showed the largest differences between active and sham conditions. White squares occur along the self-transition diagonal as well as marking transitions that never occurred or in **(D)** where no subjects were able to be used for the correlation with LC MTC (see corresponding squares in **(E)**, marked with 0s); see main text for more details.

With the heavy caveat that every 'square' in these matrices contains a different number of subjects (**Figure S2E**), we can at least conduct some qualitative explorations. The aspects to focus on are **Figure S2C** and **S2D**, which show the differences between active and sham in transition-specific pupil dilation changes as well as the correlations between these changes and LC MTC across subjects. The differences themselves (**Figure S2C**) may not appear particularly meaningful, but four correlations with LC MTC (**Figure S2D**) stand out: $S4 \rightarrow S1$, $S5 \rightarrow S4$, $S1 \rightarrow S5$, and $S3 \rightarrow S5$. Notably, three of these four ($S4 \rightarrow S1$, $S5 \rightarrow S4$, $S1 \rightarrow S5$) are the same three that showed significant differences between active and sham conditions in the RTPM analysis, and the largest one ($S5 \rightarrow S4$) is the specific pairwise transition that showed correlations with LC MTC. This is also consistent with our first observation that $S4$ average state duration (baseline corrected) significantly correlated with LC MTC as well.

Unfortunately, as mentioned above, the criteria used to define pupil dilation changes (**Supplementary Material Section S3.1**) did require us to discard a large number of subjects in many of these pairwise state transitions. We hope that this might be remedied by employing a one-hour long paradigm rather than one lasting less than 20 minutes, and by collecting data from more subjects. The chances of switching between states would increase and more subjects would survive the rejection standard consequently increasing the effect size. Nevertheless, despite this challenge we can see qualitative confirmation of the above findings, i.e. that LC MTC moderates the effectiveness of the active squeeze task driving the ease of transitioning into $S4$ (arousal state) as well as how long subjects persist in occupying $S4$ once they've arrived there (regardless of condition).

Thus, we were only able to show qualitative confirmation of the HMM brain state transition result with our pupillometry data. A likely cause of this result is the stringent criteria we adopted for including a particular instance of pupil dilation changes as a function of a specific pairwise transition (see **Supplementary Material Section S3.1**). As a result, many subjects were unfortunately excluded as they did not meet this preset criterion of remaining in the same state two TRs before or after a switch. Increasing the number of subjects would boost statistical power to detect this potentially small effect; longer scan durations may also help avoid loss of data usability. Unfortunately, it was not possible to increase the number of subjects or length of scans here, so these possibilities must be left to future studies.

However, there is another possible interpretation of this somewhat weak pupillometry finding. We opted to collect pupillometry data because it has been repeatedly shown that continuous

measures of pupil diameter throughout both resting state and task stimuli may index tonic variations in LC BOLD activity, and are less liable to trial-by-trial noise than pupil dilation locked into task-related events (Murphy et al., 2014). Further, electrophysiological studies in monkeys have often shown a reliable relationship between LC activity and changes in pupil diameter due either to spontaneous fluctuations, or to external stimuli (Joshi et al., 2016). However, evidence is now mounting that fluctuations in LC do not necessarily covary with pupil diameter in statistically meaningful ways (Megemont et al., 2022; Yang et al., 2021). It therefore seems reasonable to conclude that a lack of strong statistical support from the pupillometry analyses should not color interpretation of our primary network analysis and correlation with LC neuromelanin levels.